

LA-UR-21-30698

Approved for public release; distribution is unlimited.

Title: FY21 FINAL REPORT, NNSA-IAEC SCIENCE AREA V, ENVIRONMENTAL ISR, WASTE MANAGEMENT AND SUBSURFACE SCIENCE

Author(s): Bussod, Gilles Yves A.; Stauffer, Philip H.; Boukhalfa, Hakim; Bourret, Suzanne Michelle; Hayes-Rich, Nathan Gerald; Cockreham, Cody Blaze; Rosenzweig, Ravid; Calvo, Ran; Balaban, Noa; Klein-BenDavid, Ofra; Dixon, Paul Robert; Kiess, Thomas

Intended for: Report

Issued: 2021-11-16 (rev.1)

Disclaimer:

Los Alamos National Laboratory, an affirmative action/equal opportunity employer, is operated by Triad National Security, LLC for the National Nuclear Security Administration of U.S. Department of Energy under contract 89233218CNA000001. By approving this article, the publisher recognizes that the U.S. Government retains nonexclusive, royalty-free license to publish or reproduce the published form of this contribution, or to allow others to do so, for U.S. Government purposes. Los Alamos National Laboratory requests that the publisher identify this article as work performed under the auspices of the U.S. Department of Energy. Los Alamos National Laboratory strongly supports academic freedom and a researcher's right to publish; as an institution, however, the Laboratory does not endorse the viewpoint of a publication or guarantee its technical correctness.

FY21 FINAL REPORT
NNSA-IAEC SCIENCE AREA V
ENVIRONMENTAL ISR

WASTE MANAGEMENT AND
SUBSURFACE SCIENCE

Prepared for NNSA
Year FY21 Project Deliverable
October 28, 2021

Los Alamos National Laboratory
Gilles Y. Bussod, Philip H. Stauffer, Hakim Boukhalfa
Michelle Bourret, Nathan Hayes-Rich, Cody Cockreham

Geological Survey of Israel
Ravid Rosenzweig, Ran Calvo

Nuclear Research Center, Negev
Noa Balaban, Ofra Klein-BenDavid

Science Area V Multi-Lab Lead
Paul R. Dixon (LANL, SPO-CNP)

HQ Project Manager, NA-22
Thomas E. Kiess (NA-22)

DISCLAIMER

This information was prepared as an account of work sponsored by an agency of the U.S. Government. Neither the U.S. Government nor any agency thereof, nor any of their employees, makes any warranty, expressed or implied, or assumes any legal liability or responsibility for the accuracy, completeness, or usefulness, of any information, apparatus, product, or process disclosed, or represents that its use would not infringe privately owned rights. References herein to any specific commercial product, process, or service by trade name, trade mark, manufacturer, or otherwise, does not necessarily constitute or imply its endorsement, recommendation, or favoring by the U.S. Government or any agency thereof. The views and opinions of authors expressed herein do not necessarily state or reflect those of the U.S. Government or any agency thereof.



ACKNOWLEDGEMENTS

The authors thank our technical support staff responsible for the analytical characterization and modeling that contributed to the success of this project: George Perkins, Rose Harris, Samantha Peterson, Doug Ware and Kirsten Sauer (EES-14), for the battery of analytical measurements performed; our colleague Satish Karra (EES-16) for his guidance using FEHM and PFLOTRAN; and our Program Manager Paul Dixon (SPO-CNP, LANL) for his unwavering support.

We also acknowledge the essential contributions of our colleagues, Professors Xianghui Zhang and Di Wu from Washington State University, who provided access to their *in-situ* IR, *in-situ* XRD, and nano-CT facilities as well as their analytical expertise in interpreting the results.

CONTENTS

	Contents.....	iii
	LIST OF FIGURES.....	v
	LIST OF TABLES	vii
	ACRONYMS	viii
	ABBREVIATIONS/ UNITS	x
1	Executive Project Summary	1
2	Introduction	3
	2.1 FY21 Research Focus Areas.....	3
	2.1.1 FY21 Flow and Transport Process Modeling: In Support of SNL Safety Assessment for IBD Disposal of IAEC Nuclear Waste.....	4
	2.1.2 FY21 Experimental Geochemistry: Effects of Thermal Loading and Radiation on the Hydrogeochemical and Microstructural Evolution of the IBD Site	5
	2.1.3 FY21 Activity Summary.....	6
3	FY21 Flow and Transport Process Modeling: In Support of SNL Safety Case for IBD Disposal of IAEC Nuclear Waste.....	9
	3.1 Geological Framework Model (GFM) Update	9
	3.1.1 Changes in Geostatistical Distribution: Effect of Mishash-A LFA Inversion on Hydrologic Properties.....	10
	3.2 Hydrogeologic Flow and Reactive Transport Model Development.....	14
	3.3 Update of Initial Subsurface Water Saturation Conditions	15
	3.3.1 Steady-State Saturation Background Simulations.....	15
	3.4 Flow and Transport Models.....	18
	3.4.1 Ponding Climate Scenario Runs	19
	3.4.2 Ponding Infiltration Footprint.....	22
	3.5 Flow and Transport Simulation Results.....	23
	3.5.1 Reactive Tracer Simulations Update	23
	3.6 Heat-generating Radionuclide Waste Simulations	25
4	Experimental Geochemistry: Effects of Thermal Loading & Radiation on the Hydrogeochemical and Microstructural Evolution of the IBD Disposal of IAEC Nuclear Waste.....	32
	4.1 Introduction.....	32
	4.2 Reaction Chemistry & Kinetics of the Thermal Decomposition of Organic-rich Negev Carbonates	33
	4.2.1 Source Materials	33
	4.2.2 Analytical Methods.....	33
	4.2.3 Sample Characterization	34

4.2.4	Reaction Chemistry & Kinetics of Thermal Decomposition for Bituminous (organic-rich) Negev Carbonate Rocks.	37
4.2.5	Phase Stability and Thermally-induced Microstructural and Mineralogical Phase Changes	40
4.2.6	Chemical Reaction By-products of Bituminous Negev Carbonates During Progressive Heating	46
5	Summary and Conclusions.....	50
6	References	53
7	FY21 Meetings and Publications	54
7.1	Meetings and Publications	54
7.1.1	Annual Workshops	54
7.1.2	Weekly and bi-Monthly Meetings.....	54
7.1.3	Publications.....	55

LIST OF FIGURES

Figure 2-1. 2017-2021 Development of Integrated, Coupled 2D and 3D F&T Process Models for the Northeastern Negev Subsurface.	7
Figure 3-1. New Geostatistical distribution of lithofacies assemblages (LFAs) with respect to HFUs. The FY21 changes involve the 24 m thick Mishash-A HFU only, where the phosphorite LFA now overlies the chert LFA.....	11
Figure 3-2. Comparison of permeability and porosity fields for (a) previous October 2020 flow and transport model, and (b) the new 2021 version where the chert and phosphorite layers have been flipped within the Mishash-A HFU (z = 215 – 239 m; red arrow range).....	12
Figure 3-3. Example of 4 distinct geostatistical realizations for Menuha Formation porosity distribution. The distribution of porosity values within a same LFA used in geostatistical analysis varies for the same input values (see text). Shown are XY slices of the Menuha layer from the same 205 m elevation.	13
Figure 3-4. 2D Slice of 3D present-day model of initial Negev subsurface liquid saturation state. High saturation is shown in blue and low saturation is red.	16
Figure 3-5. Saturation profile along the vertical z-axis of the IBD for the 3D heterogeneous property distribution model (gray line) versus the saturation profile of the 1D model (blue line) and field saturation data from Negev desert wells (red asterix).	17
Figure 3-6. 3-D Computational IWD Domain (100m ² x 160m) with Seven Hydrofacies Units (HFUs).....	18
Figure 3-7. Top view of the ponding zone (50 m x 50 m) at Top of Hazeva Gr. alluvial sediments.....	19
Figure 3-8. Saturation profile along z-axis at x = 0 m, y = 0 m for background and ponding at 50 days (left), and 150 years (right).	20
Figure 3-9. Saturation profile along x-axis at y = 0 m, z = 332 m for background and pond at 150 years.....	21
Figure 3-10. Saturation profile along z-axis at x = 0 m, y = 0 m for background and pond at 200 y.	21
Figure 3-11. Saturation profile along x-axis at y = 0, z = 332 for background and pond at 200 y.	22
Figure 3-12. Total dissolved uranium for four infiltration scenarios after 100 years.....	24
Figure 3-13. Dissolved ²³⁵ U tracer migration for 30 mm/y infiltration scenario through time.	25
Figure 3-14. Step-linear energy source (blue) vs. half-life decay energy source (red).	26
Figure 3-15. Temperature profile along z-axis at x = 0, y = 0 for both heat sources at 25 y (left), and plot showing temperature distribution across a slice of the model domain for the decaying heat source (right).	26
Figure 3-16. Temperature profile at 25 y (left) vs. the specific heat profile (right).	27
Figure 3-17. Temperature profile at 25 y (left) vs. the thermal conductivity profile (right).	28

Figure 3-18. Temperature profile along z-axis at x = 0 m, y = 0 m for both heat sources at 200 y.	28
Figure 3-19. Results of the temperature of the nodes adjacent to the borehole (x = 2 m, y = 0 m) for the decaying heat source scenario for 5 and 50 years following source introduction.	29
Figure 3-20. Saturation versus time on nodes adjacent to the borehole (x = 2 m, y = 0 m) for the 40 GWd/mT heat source.....	30
Figure 3-21. Temperature versus time on nodes adjacent to the borehole (x = 2 m, y = 0 m) for the 40 GWd/mT heat source.....	30
Figure 3-22. Saturation versus time to 0.2 years on nodes adjacent to the borehole (x = 2 m, y = 0 m) for the 40 GWd/mT heat source.....	31
Figure 4-1. Quantitative X-ray diffraction refinement of OS-2. Corundum content of 20 wt.% added. Refinement parameters: $R_{wp} = 4.11$, $R_{exp} = 2.19$, $X^2 = 3.52$, GoF = 1.88.	34
Figure 4-2. Quantitative X-ray diffraction refinement of OS-3. Corundum content of 20 wt.% added. Refinement parameters: $R_{wp} = 3.51$, $R_{exp} = 2.42$, $X^2 = 2.10$, GoF = 1.45.	34
Figure 4-3. Quantitative X-ray diffraction refinement of OS-4. Corundum content of 20 wt.%. Refinement parameters: $R_{wp} = 3.17$, $R_{exp} = 2.19$, $X^2 = 2.10$, GoF = 1.45.	35
Figure 4-4. Quantitative X-ray diffraction refinement of HOP-5. Corundum content of 20 wt.% added. Refinement parameters: $R_{wp} = 3.26$, $R_{exp} = 2.22$, $X^2 = 2.16$, GoF = 1.47.	35
Figure 4-5. Thermogravimetry and derivative thermogravimetry (TG-DTG) from 30°C to 1100°C at a scan rate of 10°C/min in argon, (a) OS-2, (b) OS-3, and (c) OS-4, and (d) HOP-5.....	37
Figure 4-6. Differential scanning calorimetry (DSC) from 30°C to 1100°C at a scan rate of 10°C/min in argon; (a) OS-2, (b) OS-3, and (c) OS-4, and (d) HOP-5.....	38
Figure 4-7. Mass spectrometry from 30°C to 1100°C at a scan rate of 10°C/min in argon, (a) OS- 2, (b) OS-3, and (c) OS-4, and (d) HOP-5.	39
Figure 4-8. In-situ X-ray diffraction (in situ XRD) pattern of OS-2, range of 2 θ of 5-80°, from 35°C to 600°C in argon.....	41
Figure 4-9. <i>In-situ</i> X-ray diffraction (in situ XRD) pattern of OS-3, range of 2 θ of 5-80°, from 35°C to 600°C in argon.....	42
Figure 4-10. <i>In-situ</i> X-ray diffraction (in situ XRD) pattern of OS-4, range of 2 θ of 5-80°, from 35°C to 600°C in argon.....	43
Figure 4-11. In-situ X-ray diffraction (in situ XRD) pattern of HOP-5, range of 2 θ of 5-80°, from 35°C to 600°C in argon.....	44
Figure 4-12. 3D plots of in-situ X-ray diffraction (in-situ XRD) patterns, 2 θ of 5-80°, from 35°C to 600°C in argon: Samples OS-2 (a), OS-3 (b), OS-4 (c), and HOP-5 (d); (e) 3D plot of 2 θ of 26°-35° showing the OS-3 (104) peak for calcite ($CaCO_3 = 54$ wt.%); (f) Normalized integration of intensity (NIoI) from all the samples (104) peak for calcite.....	45
Figure 4-13. In-situ diffuse reflectance infrared Fourier transform spectroscopy (in-situ DRIFTS) spectra from 35°C to 600°C in helium for Negev bituminous carbonate samples OS-2 (a), OS-3 (b), OS-4 (c) and HOP-5 (d).....	47
Figure 4-14. <i>In-situ</i> DRIFTS spectra from 35°C to 600°C in helium for Negev bituminous carbonate samples OS-2 (a), OS-3 (b), OS-4 (c) and HOP-5 (d).....	49

LIST OF TABLES

Table 2-1. Waste Management Research Topics in Science Area V.	8
Table 3-1. Thicknesses of Lithologic Units for Each HFU. Note that the phosphorite and massive chert lithofacies have been inverted compared to the configuration used in the 2017-2020 Final Report (LA-UR-20-28271).	9
Table 3-2. Geostatistical Parameters Used in GSLIB. From Bussod <i>et al.</i> (2020).	14
Table 3-3. Summary of Hydrologic Properties for Negev Samples HOP-5, CK-6, LS-12, CL-8, SS-10 (from 2017-2020 Final Report, (Bussod <i>et al.</i> , 2020). Saturated hydraulic conductivity (Ksat) was measured using <i>Falling-Head Rising-Tail Flexible Wall</i> method (Bussod <i>et al.</i> , 2020, Appendix A). van Genuchten parameters for unsaturated samples were calculated using the RETC code (van Genuchten <i>et al.</i> , 1991) to fit the measured moisture retention points and characteristic curves for hydraulic functions (i.e., relative permeability and capillary pressure).	23
Table 4-1. Inorganic and Organic Phase Contents of Negev Samples. Determined from quantitative X-ray diffraction (qXRD), thermogravimetric analysis (TG), and total organic carbon (TOC) measurements.....	36

ACRONYMS

c.f.	compare (<i>conferatur; latin</i>)
DRIFTS	<i>in-situ</i> diffuse reflectance infrared Fourier Transform spectroscopy
DSC	Differential Scanning Calorimetry
DTG	Derivative thermogravimetric analysis technique
e.g.	for example (<i>exempli gracia; latin</i>)
<i>et al.</i>	and others (<i>et alius; latin</i>)
F&T	Flow and Transport (model or code)
FEHM	Finite Element Heat and Mass Transfer code
Fm.	Geologic Formation
FY	Fiscal Year
GFM	Geologic Framework Model
Gr.	Geologic Group
GSLIB	FORTRAN library of scripts
GSI	Geological Survey of Israel
HFU	Hydrofacies Units
HOP-5	Bituminous phosphorite
IAEC	Israel Atomic Energy Commission
IBD	Intermediate borehole disposal
i.e.	<i>that is (id est; latin)</i>
Ksat	Saturated hydraulic conductivity
Kd	Sorption Coefficient
LANL	Los Alamos National Laboratory
LFA	Lithofacies Assemblage
LLNL	Lawrence Livermore National Laboratory
MS	Mass spectrometry
Nano-CT	nano-computed tomography imaging technique
NE	Northeast cardinal direction
NNSA	U.S. National Nuclear Security Administration
NIoI	Normalized the integration of intensity
NRCN	Nuclear Research Center – Negev
OS-2,3,4	Bituminous carbonate marls
PFLOTTRAN	Flow and Transport code
qXRD	Quantitative X-ray diffraction
TG	Thermogravimetric

TG-DSC	Thermogravimetric and differential scanning calorimetry
TOC	Total organic carbon
SEM	Scanning electron microscopy
SNL	Sandia National Laboratory
²³⁵ U	Isotope of Uranium
WM3/5/7	Waste Management Research Topic 3,5,7
XRF	X-ray fluorescence
XRD	X-ray diffraction
YP	Yamin Plain (NE Negev Desert)
1D/2D/3D	Two Dimensional/Three Dimensional

ABBREVIATIONS/ UNITS

°C	Degrees Celcius
cm	Millimeter
d	day
GWd/mT	Giga Watts day per metric ton
kg	Kilogram
km	Kilometer
kW	Kilowatt
m	Meter
L	Liter
m	Meter
Ma	Million years
min	Minute
mL	Milliliter (also ml)
mm	Millimeter
m/z	Normalized atomic mass
mL	Milliliter (also ml)
mm/y	Millimeters per year
pH	Measure of acidity or alkalinity of a solution
s	Second
W/(m.K)	Watts per (meter x degrees Kelvin)
wt. %.	Weight percent
y	Year
%	Percent

This page is intentionally left blank.

2021 LANL FINAL REPORT

NNSA-IAEC SCIENCE AND TECHNOLOGY WORKING GROUP
SCIENCE AREA V
BASIC SCIENCE OF WASTE MANAGEMENT & SUBSURFACE SCIENCE

Waste Management Research Topic 3 (WM3)
Mechanisms of Subsurface Radionuclide Transport

1 Executive Project Summary

The FY21 NNSA NA-22 Final Report represents the progress achieved over the past year (FY21) by the research team for Topic Area 3, *Waste Management & Subsurface Science* (WM3), and Topic Area 7, *Radiation and Thermal Effects on Bituminous Rocks* (WM7). WM3 and WM7 are part of Science Area V (*Subsurface Science and Waste Management*) in the NNSA-IAEC Science and Technology Working Group. The project was initiated four years ago (2017) with an MOU agreement between the U.S. National Nuclear Security Administration (NNSA) and the Israel Atomic Energy Commission (IAEC) to evaluate the feasibility of geological subsurface disposal of radioactive waste in Israel. The core WM3 and WM7 teams are comprised of scientists and engineers from Los Alamos National Laboratory, the Geologic Survey of Israel (GSI), and the Nuclear Research Center - Negev (NRCN), with a close collaboration to the teams from Sandia National Laboratory (SNL) and Lawrence Livermore Laboratory (LLNL).

Prior research findings (2017-2020) by the WM3 team are presented in the 2017-2020 Science Area 5 NNSA-IAEC Final Report (Bussod *et al.*, 2020). These were initially focused around the siting of a potential underground *Geologic Repository System* in the Northeastern Negev desert, Israel, and subsequently changed to the construction of an *Intermediate Borehole Disposal* (IBD) radioactive waste site (2020).

Having successfully completed a 3-year integrated program, in FY21 we refocused our work around two major activities related only to an IBD waste site in the northeastern Negev. These activities included (1) a *Flow and Transport (F&T) Process Modeling Program*, in support of the SNL Safety Case for IBD disposal of IAEC nuclear waste (Task 1; Section 3), and (2) an *Experimental Geochemistry Program* on the effects of thermal loading and radiation on the hydrogeochemical and microstructural evolution of the IBD Site (Task 2; Section 4).

As of result of our FY21 studies we have confirmed that:

1. The Late Cretaceous shallow marine rock sequence of the Northeastern Negev, Israel, in which the IBD has been proposed to be sited, constitutes a potentially robust “natural barrier” to subsurface radionuclide contaminant migration and is the key to nuclear waste containment for a Negev subsurface waste disposal system.
2. In this Negev desert rock sequence, the major radionuclide-sorbing mineral phases responsible for the mitigation contaminant plume migration are montmorillonitic clays in bituminous limestone marls and carbonated calcium fluoroapatite in phosphorites.
3. In the absence of thermal loading, updated FY21 Flow and Transport model simulations designed to assess the potential impact of future climate change scenarios on IBD disposal indicate that
 - a. For future, wetter climate scenarios, extreme infiltration conditions (210 mm/y), and failed IBD waste package containment, the nuclear inventory may be swept out of the near field domain (80 m x 100 m x 100 m) in just over 200 years.
 - b. For similar wetter climate scenarios involving more moderate infiltration conditions (30 mm/y), the contaminant plume remains within the IBD domain even after 1000 years.
 - c. For ponding events, assuming a present-day infiltration rate (0.1 mm/y), and an IBD early contaminant breach of the entire IBD inventory and occurs early, a radioactive plume could escape the nearfield domain after 700 years but at concentrations values that would likely be undetectable.

Given the preponderance of hydrocarbon-rich rocks in the Negev “*natural barrier*” system, the effects of thermal loading and radiation from the IBD site may have drastic consequences for radionuclide containment and/or migration. Our early FY21 geochemistry results on the temperature-dependent breakdown of organic-rich Negev lithologies suggests exceeding temperatures of 250-300°C may trigger decomposition reactions and microstructural damage in the IBD near field. Further experimental studies on thermal loading and radiation effects are planned for FY22-23.

In FY21 we have updated our Negev F&T subsurface model to simulate IBD thermal loading and predict the evolution of subsurface temperature profiles over time. Combined with the new experimental constraints on temperature and radiation effects, in FY22-23, we will be able to (i) investigate and predict changes in subsurface properties (e.g., hydrologic flow pathways and

geochemical sorption), and (ii) evaluate the efficacy of the natural barrier system subjected to an nuclear waste IBD for the Northeastern Negev site.

2 Introduction

This NNSA NA-22 Final Report represents the progress achieved over the past year (FY21) by the research teams for Topic Area 3, *Waste Management & Subsurface Science* (WM3), and Topic Area 7, *Radiation and Thermal Effects on Bituminous Rocks* (WM7). WM3 and WM7 are part of Science Area V (*Subsurface Science and Waste Management*) in the NNSA-IAEC Science and Technology Working Group. The project was initiated four years ago (2017) with an MOU agreement between the U.S. National Nuclear Security Administration (NNSA) and the Israel Atomic Energy Commission (IAEC) to evaluate the feasibility of geological subsurface disposal of radioactive waste in Israel. The WM3 and WM7 teams are comprised of scientists and engineers from Los Alamos National Laboratory, the Geologic Survey of Israel (GSI), and the Nuclear Research Center - Negev (NRCN), with a close collaboration with the teams from Sandia National Laboratory (SNL) and Lawrence Livermore Laboratory (LLNL).

2.1 FY21 Research Focus Areas

Prior research findings (2017-2020) by the WM3 team are presented in the 2017-2020 Science Area 5 NNSA-IAEC Final Report (Bussod *et al.*, 2020). These were initially focused (2017-2019) around the siting of a potential underground *Geologic Repository System* in the Northeastern Negev desert, Israel, and subsequently changed to the construction of an *Intermediate Borehole Disposal* (IBD) radioactive waste site (2020). From 2017-2020 our research was centered around 3 parallel activities:

- *Geologic Subsurface Characterization: Northeastern Subsurface Geologic Framework Model* (Task 1).
- *Flow and Transport (F&T) Process Model Development: 3D Regional- and Site-scales* (Task 2).
- *Experimental Geochemistry: Uranium Sorption Equilibrium and Surface Complexation Models* (Task 3).

Having successfully completed a 3-year integrated program, in FY21 we refocused our work around two major activities related only to an *Intermediate Borehole Disposal* (IBD) waste site in the northeastern Negev. These activities included:

- *Flow and Transport (F&T) Process Modeling: In Support of SNL Safety Assessment for IBD Disposal of IAEC Nuclear Waste* (Task 1; Section 3).

- *Experimental Geochemistry: Effects of Thermal Loading and Radiation on the Hydro-geochemical and Microstructural Evolution of the IBD Site* (Task 2; Section 4).

2.1.1 *FY21 Flow and Transport Process Modeling: In Support of SNL Safety Assessment for IBD Disposal of IAEC Nuclear Waste.*

In this work we aim to address (i) subsurface processes at the site-scale, in the vicinity of an IBD waste package, and (ii) the coupled effects of heat and radiation on the hydrologic, geochemical and thermal evolution of the nearfield. This effort is supported by 2D and 3D subsurface computational meshes developed at LANL between 2017 and 2020, in collaboration with colleagues from the Geological Survey of Israel (GSI) and the Nuclear Research Center - Negev (NRCN).

Last year (FY20), we used FEHM and PFLOTTRAN codes for regional and site-scale F&T simulations to model the saturation of the Yamin Plain subsurface down to 500 m depth, under past Glacial Period conditions (10,000 years ago), and present-day Post-glacial arid environments (Bussod *et al.*, 2020). We also implemented an equilibrium uranium sorption model based on the results from three years of uranium sorption and kinetic laboratory experiments conducted by the LANL geochemistry team from 2017-2020. These simulations were performed at current low-infiltration fluxes and under several future “wetter” climate scenarios with greatly increased infiltration, and offer us a glimpse into the potential actinide sorption capacity of the Negev subsurface in the absence of thermal loading or radiation effects. The models also predict potential pathways for radioactive plume migration away from the IBD site in the absence of major fault or fracture zones.

This past year (FY21) we investigated the issue of thermal loading by adding a “generic *Used Fuel* heat source” to our FEHM and PFLOTTRAN F&T codes. Presented in this FY21 report are preliminary simulations on the coupled temperature and saturation effects of thermal loading by IBD waste packages. To accomplish this we:

- Updated of our FY20 Geological Framework Model (GFM) and the subsurface hydro-stratigraphy and lithofacies assemblages (LFAs) using new 2021 data provided by our colleagues from the Geological Survey of Israel (GSI). As reported in Section 3.1 below, this has resulted in improvements in our geostatistical representations of:
 - *The layered lithologic sequences (e.g., distribution and variability of rock types),*
 - *Hydrologic property distributions (e.g., porosity, permeability) and,*
 - *Geochemical property distributions (e.g, radionuclide sorption potential) in the vicinity of the proposed IBD.*

- Re-evaluated the initial subsurface water saturation conditions using the updated GFM and new NRCN and GSI infiltration values for the Negev desert region from new near surface borehole data and paleoclimate data (Section 3.2).
- Developed and implemented 2D and 3D thermal loading models using FEHM and PFLOTTRAN codes to evaluate the effects of heat-generating waste packages in the Yamin Plain subsurface around the IBD (Section 3.3). In the absence of specific or new data, we used thermal loading values for Used Fuel waste derived from the literature (Carter *et al.*, 2012) using rock thermal conductivity values measured on Negev carbonate lithologies by Sandia National Lab and GSI colleagues a (Bauer *et al.*, 2021; Itay Reznik, GSI, pers. Comm.). This work encompasses modeling the time- and temperature-dependent evolution of subsurface conditions (e.g., saturation, temperature) due to thermal loading in the nearfield region of the IBD location.

2.1.2 FY21 Experimental Geochemistry: Effects of Thermal Loading and Radiation on the Hydrogeochemical and Microstructural Evolution of the IBD Site

In FY20, we completed a 3-year experimental lab study on the uranium sorption potential of Negev carbonate lithologies at saturated conditions. From this work we determined the apparent equilibrium sorption coefficients (K_d) for uranium sorption for 6 Negev lithologies and developed a uranium surface complexation model that was parameterized for inclusion in 2D and 3D flow and transport simulations. Results of the tests and model results were reported in the 2017-2020 NNSA Final Report (Bussod *et al.*, 2020).

In FY21, the program was refocused to address the effect of temperature on the stability of Late Cretaceous shallow marine-deposited, organic-rich rocks that are co-located with the proposed IBD in the depth range of 100 m to 300 m. The FY21 chemistry analysis performed at LANL directly addresses concerns related to the breakdown and remobilization of hydrocarbon phases (i.e., gas and liquid phases) in the vicinity of a subsurface nuclear waste borehole disposal facility. When completed, this study will also provide quantitative data for assessing the effect of heating on changes in porosity, permeability and hydraulic conductivity of Negev lithologies over time. The experimental data will inform model parameters and semi-empirical equations that can be input into our flow and transport process models. Geochemical, analytical and experimental activities this year were centered on:

- The reaction chemistry and kinetics of thermal decomposition of bituminous (organic-rich) Negev carbonate rocks subjected to thermal loading from subsurface IBD waste disposal.
- Determining the phase stability and thermally induced phase changes affecting the modal mineralogy and microstructural textures of organic-rich Negev lithologies using

quantitative X-ray Diffraction (QXRD), and thermogravimetric and differential scanning calorimetry (TG-DSC).

- Measuring the types of chemical byproducts formed from bituminous Negev carbonate rocks during progressive heating up to 1000°C, using in-situ diffuse reflectance infrared Fourier Transform spectroscopy (DRIFTS).

2.1.3 FY21 Activity Summary

The ultimate objective of these studies is to provide quantitative experimental constraints and semi-empirical equations for input into the subsurface flow and transport process model(s) that serve as a scientific basis for the IBD waste disposal *Safety Case*.

Since 2017 the WM3 Topic Area Team focused on Mechanisms of Subsurface Radionuclide Transport and has developed the first subsurface flow and transport models for the Northeastern Negev Desert in Israel. This was accomplished by integrating our collaborative NNSA-IAEC work around 3 activities that include (i) a Negev desert *Subsurface Characterization Task 1* (Field Geology & Geophysics Program), (ii) an *Experimental and Analytical Geochemistry Task 2* (Geochemistry Program), and (iii) a *Flow and Transport Modeling Task 3* (Hydrogeology Program) (**Figure 2-1**).

This integration has resulted in:

- Task 1 – 3D subsurface Geologic Framework Model (GFM).
- Task 2 – Uranium equilibrium- and analytical surface complexation - models.
- Task 3 – 2D and 3D Flow and Transport (F&T) regional-scale and IBD site-scale models.

At a minimum this data should more realistically capture changes in the nearfield region of heat-generating IBD rad-waste packages. This includes:

- Major dynamic response processes (c.f., phase changes, gas generation, fluid migration, recrystallization).
- Potential hydro-geochemical evolution of the subsurface (c.f., saturation, groundwater chemistry, fracture healing/generation).
- Potential effect of thermal loading, radiation and climate change on properties (c.f., porosity, relative permeability, thermal conductivity, radioactive plume migration pathways).

We have successfully initiated and carried out all studies planned for FY21 however, at this stage the majority of our results are only preliminary and will be verified and validated in FY22-23. Specifically, all thermal modeling (WM3) and laboratory test results on bituminous marl (WM7)

have yet to be thoroughly analyzed, quantified, and integrated with the PFLOTRAN subsurface process model which we intend to use as input to the SNL *Safety Case / Performance Assessment* activity of WM5 (Table 2-1).

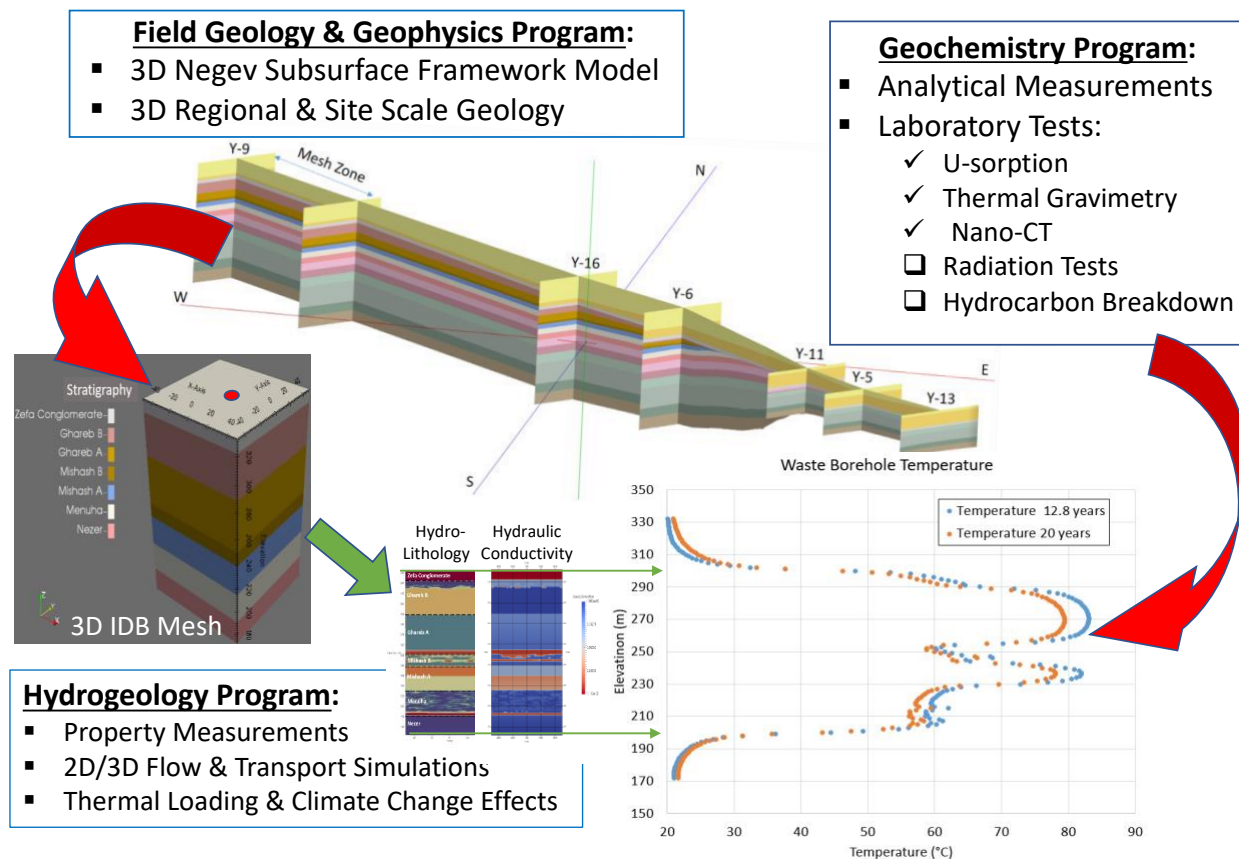


Figure 2-1. 2017-2021 Development of Integrated, Coupled 2D and 3D F&T Process Models for the Northeastern Negev Subsurface.

In FY22-23, in parallel with continued work on thermal loading effects (WM3), the experimental geochemistry program will initiate laboratory tests on the potential for radiation damage and effects on phase stability and potential migration of organic-rich phases in bituminous Negev carbonate lithologies (WM7).

In light of our FY21 findings, future work planned for 2022-2023 will include the model integration of the thermal and radiation effect(s) of IBD of nuclear waste with coupled heat-mass-flow-radiation F&T model simulations. In collaboration with our Israeli colleagues from GSI and NRCN, we are gathering data that may serve to predict property changes due to the potential thermal breakdown and radiation damage on Negev organic-rich LFAs and the resulting remobilization of hydrocarbon fluids in bituminous rock around the IBD.

Research Topic Abbreviation	Research Topic Name	Started	Expected outcome
WM1 (SNL Lead)	Thermomechanical damage	Since 2017	Initiate experiments & modeling on shallow marine sediments of the NE-Negev Desert lithostratigraphy
WM2 (LLNL Lead)	Colloid facilitated transport	Since 2017	Experiments & modeling radionuclide contaminant & colloid transport in the vadose zone.
WM3 (LANL Lead)	Mechanisms of radionuclide transport	Since 2017	Development of the vadose zone flow & transport model for the NE Negev Desert & refinement, accounting for new experimental and field surface fracture data.
WM4 (Vanderbilt/SNL Lead)	Waste form interactions with geological strata	Since 2018	Experiments & modeling to assess thermal & microbial effects on waste forms and waste containers.
WM5 (SNL/ Lead)	Borehole disposal of radioactive waste in Israel	Since 2019	Development of pre-closure & post-closure safety assessments for intermediate borehole disposal (IBD).
WM7 SNL/LLNL/LANL	Radiation and thermal effects on bituminous rocks	NEW FY20	Experimental data to constrain WM3 & WM5 calculations related to the Safety Case.

Table 2-1. Waste Management Research Topics in Science Area V.

3 FY21 Flow and Transport Process Modeling: In Support of SNL Safety Case for IBD Disposal of IAEC Nuclear Waste

3.1 Geological Framework Model (GFM) Update

Prior to implementing thermal loading simulations and initiating new F&T realizations we incorporated changes in our Northeastern Negev GFM model based on suggestions from our Israeli colleagues (Rani Calvo, GSI; *pers. Commun.*, 2020). Specifically, the hydro-stratigraphic sequence of the Mishash-A hydrofacies unit (HFU) based on rock core assemblages from the Y-16 borehole and presented in the 2017-2020 Final Report (Bussod *et al.*, 2020), did not agree with stratigraphic reconstructions of the Negev subsurface based on outcrop and well data located to the north of the Yamin Plain. We therefore decided to change the lithologic sequence in the Mishash-A by inverting the phosphorite at the base (Y-16 data) with the chert layer above it. In the new representation, the layer is now 11 meters thick and overlays a massive 13 meter thick chert bed (**Table 3-1**). The overall thickness (24 m) of the Mishash-A however remains unchanged.

Table 3-1. Thicknesses of Lithologic Units for Each HFU. Note that the phosphorite and massive chert lithofacies have been inverted compared to the configuration used in the 2017-2020 Final Report (LA-UR-20-28271).

Lithology	Lithology Thickness (m)	Hydrofacies Units (HFU)	HFU Thickness (m)
Conglomerate	10	ZEFA Conglomerate	10
Limestone	5	GHAREB B	33
Chalk	4		
Marl	24		
Bituminous Marl	36	GHAREB A	39
Sandstone	3		
Chert	5	MISHASH B	11
Bituminous Marl	1		
Sandstone	2		
Bituminous Marl	3		
Phosphorite	11	MISHASH A	24
Chert	13		
Chalk	19	MENUHA	24
Limestone	2		
Marl	2		
Conglomerate	1		
Limestone	20	NEZER	20

Although the Mishash-A is only 24 meters in thickness, the large difference in the lithologic and hydro-geochemical property distributions between the low porosity, low permeability, and low radionuclide sorption capacity of the fractured chert layer and the highly porous, high permeability, and very high rad-sorption capacity of the phosphorite layer may strongly affect the state of saturation, flow pathways and radionuclide sorption effectiveness of the Mishash-A. All of new FY21 subsurface saturation state and thermal loading realizations presented in this report use the newly modified GFM though the determination of its overall effect on performance awaits further analysis. In future realizations, the two different lithologic configurations for the Misash-A will be included in the geostatistical property distributions to assess variations in the actinide sorption potential of the Mishash-A HFU.

3.1.1 Changes in Geostatistical Distribution: Effect of Mishash-A LFA Inversion on Hydrologic Properties.

In response to the modifications made to the LFA distributions in the Mishash-A HFU (depth range 215-239 m; **Figure 3-1**), changes to the full workflow were implemented prior to any new FY21 simulations. These changes included (i) geostatistical realizations to generate new porosity and permeability fields (**Figure 3-2**), and (ii) new PFLOTRAN and FEHM code input files to assign appropriate transport properties. **Figure 3-2** is a comparison of the porosity and permeability fields for the site model prior to (2020 version), and after (2021 version) the updated the lithostratigraphy.

Following changes to the Mishash-A, geostatistical models for property distributions within each HFU within the site scale model were recreated using GSLIB, a Fortran library of scripts used for geostatistic computations. As in FY20, variograms were constructed for 5 of the 7 stratigraphic layers. Whereas the bounding top Zefa Fm. conglomerate layer, and the bottom Nezer Fm. limestone layer are kept uniform due to their relatively uniform properties in the area of interest, all other layers include variograms constructed from borehole data and fit using functions within GSLIB. The reader is referred to the 2017-2020 Final Report (Bussod *et al.*, 2020) for details.

An example of the new outputs from these geostatistical realizations are shown in **Figure 3-3** for the Menuha Fm. that represents 4 distinct geostatistical realizations for porosity distribution based on the variogram for that HFU using horizontal and vertical correlation lengths (**Table 3-2**; Bussod *et al.*, 2020).

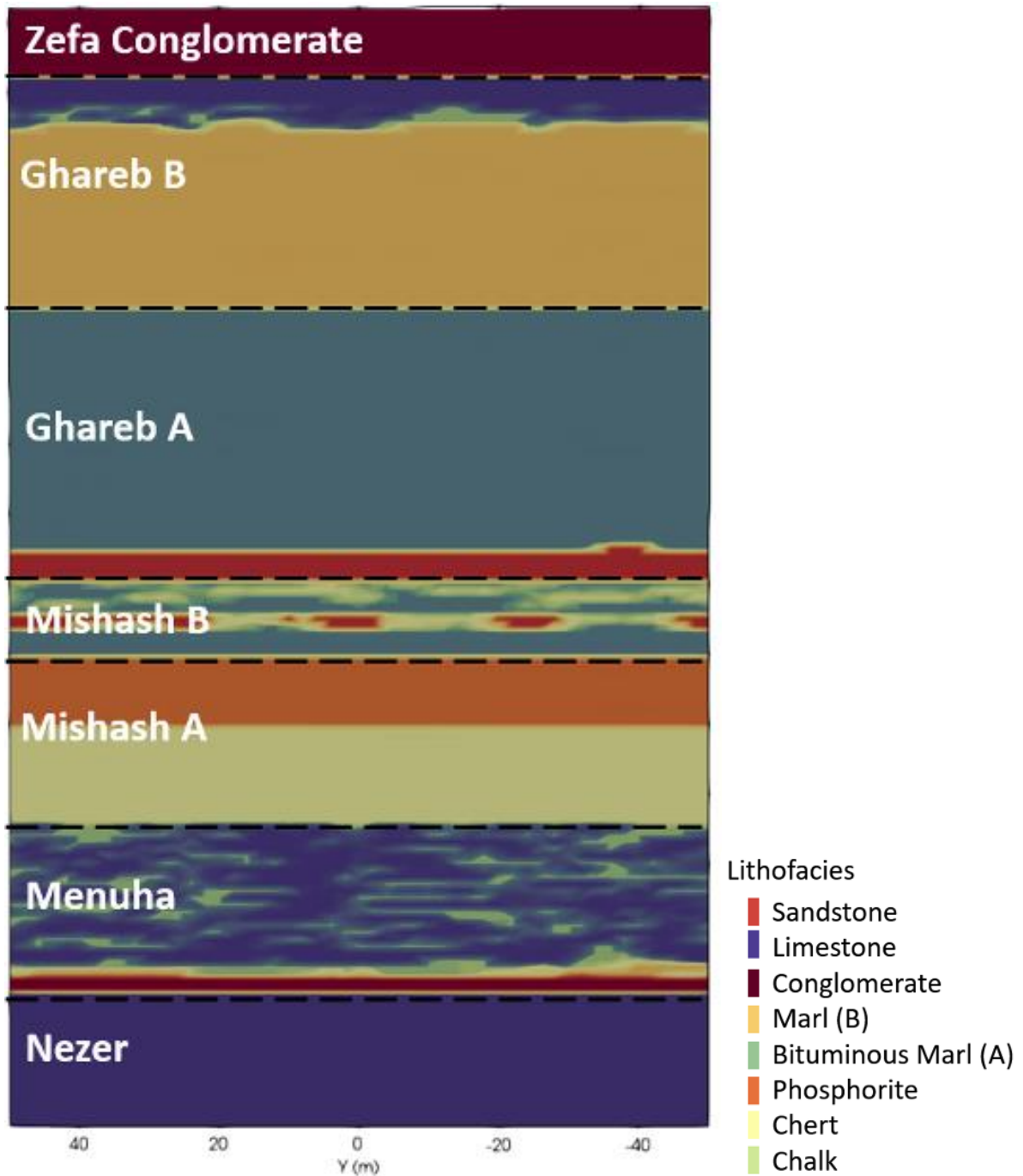
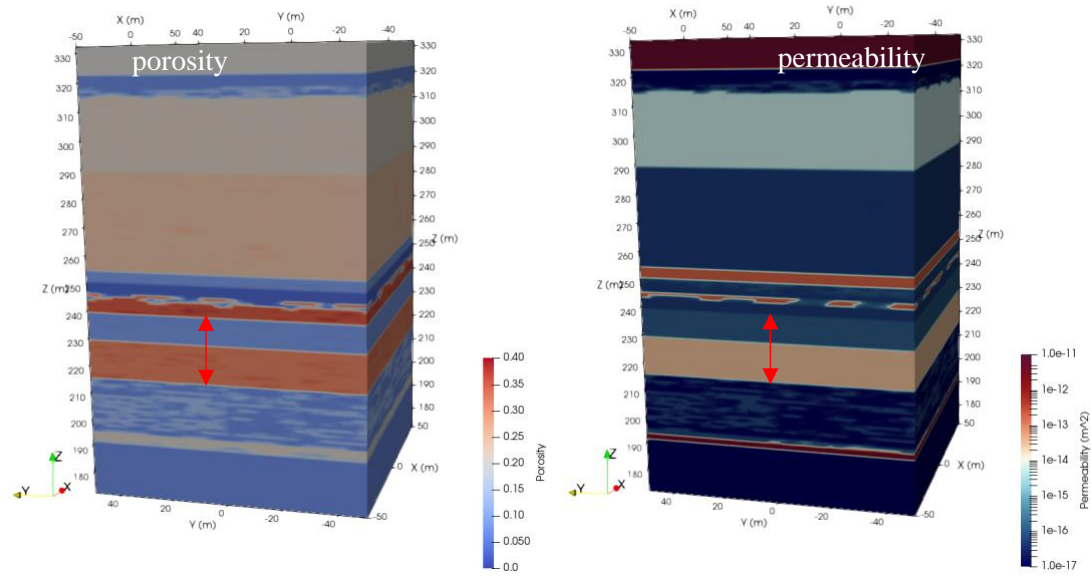
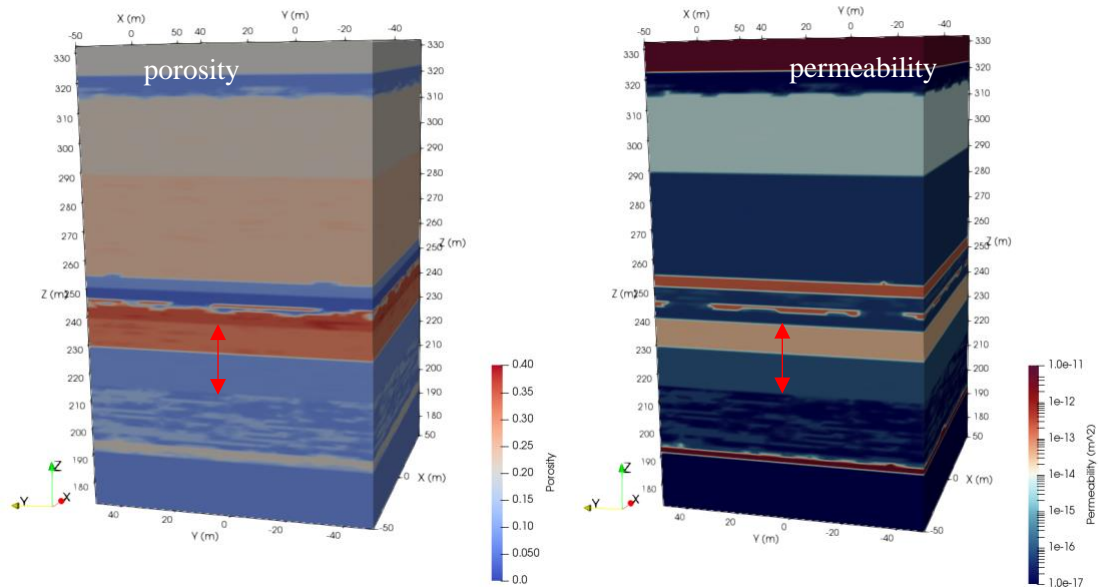


Figure 3-1. New Geostatistical distribution of lithofacies assemblages (LFAs) with respect to HFUs. The FY21 changes involve the 24 m thick Mishash-A HFU only, where the phosphorite LFA now overlies the chert LFA.



a. October 2020 version



b. October 2021 version

Figure 3-2. Comparison of permeability and porosity fields for (a) previous October 2020 flow and transport model, and (b) the new 2021 version where the chert and phosphorite layers have been flipped within the Mishash-A HFU ($z = 215 - 239$ m; red arrow range).

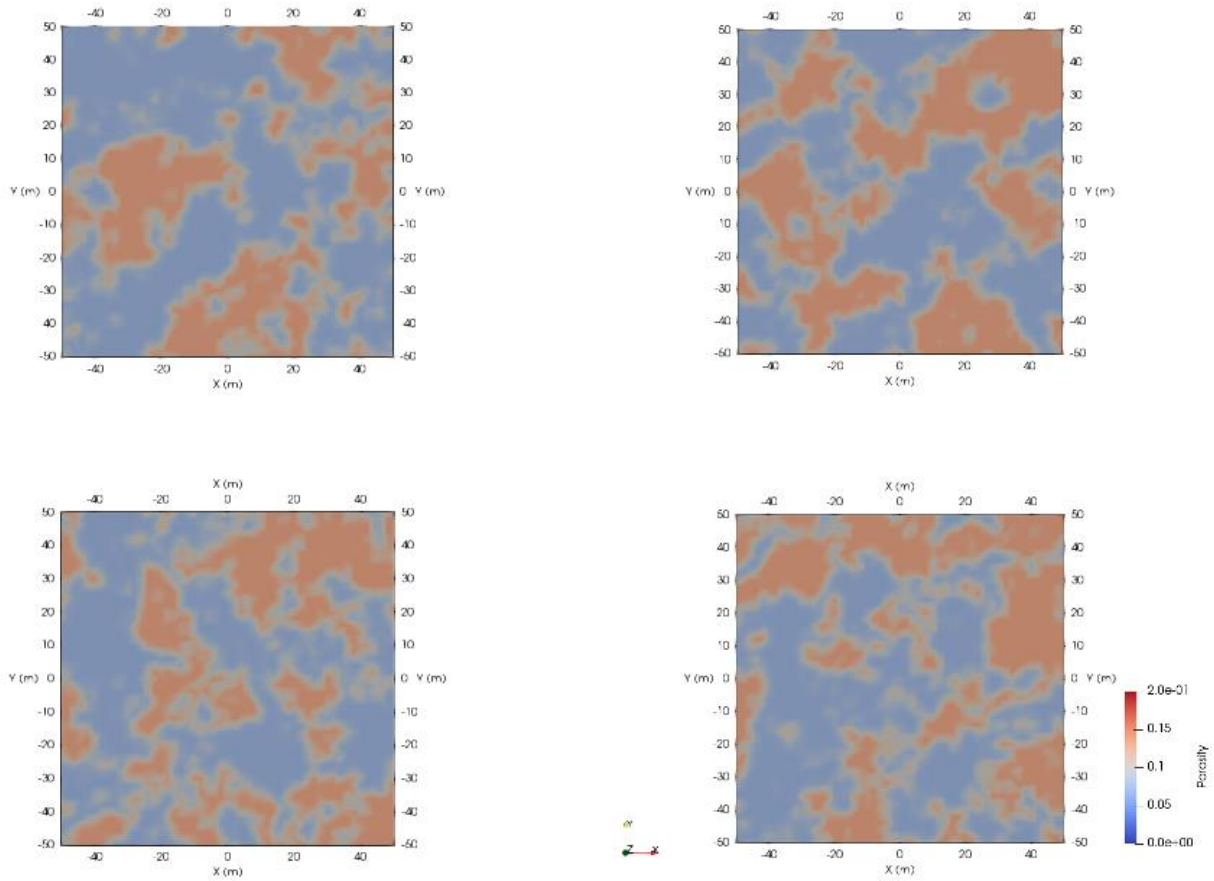


Figure 3-3. Example of 4 distinct geostatistical realizations for Menuha Formation porosity distribution. The distribution of porosity values within a same LFA used in geostatistical analysis varies for the same input values (see text). Shown are XY slices of the Menuha layer from the same 205 m elevation.

For each HFU, the multiple LFAs contained are transformed into a single function, similar to a convolution, allowing the different LFAs to interact with each other to create the patterns seen in **Figure 3-4**. Correlation lengths in the vertical direction are calculated from data in the Y-16 borehole descriptions and allowed to vary between a minimum correlation length of 1 m and maximum of 500 m (**Table 3-2**). Additionally, in the lithofacies model, each material property is allowed to vary $\pm 10\%$ from its base value.

Table 3-2. Geostatistical Parameters Used in GSLIB. From Bussod *et al.* (2020).

	Variogram Models	C parameter	Horizontal Correlation Min	Horizontal Correlation Max	Vertical Correlation
Zefa Conglomerate	CONSTANT				
Ghareb B	Exponential	0.15	1	500	15
	Hole Effect	0.3	1	500	11.9
	Hole Effect	0.4	1	500	23.5
Ghareb A	Spherical	0.1	10	500	20
	Hole Effect	0.45	50	500	6.4
Mishash B	Spherical	1.35	1	500	14
	Hole Effect	0.3	1	500	6.3
	Hole Effect	0.12	1	500	12.6
Mishash A	Spherical	0.65	1	500	10
	Hole Effect	0.08	1	500	6
	Hole Effect	0.1	1	500	9.5
Menuha	Gaussian	1	1	500	30
	Exponential	1	1	500	40
Nezer	CONSTANT				

3.2 Hydrogeologic Flow and Reactive Transport Model Development

This section describes the creation of a hydrogeologic flow and transport model. The goal of the hydrogeologic flow and transport model is to simulate the flow of water from the land surface and chemicals from the disposal borehole horizon as they migrate to depth.

The hydrogeological flow and reactive transport model includes several components:

- (1) A computational mesh, created by using the layering from the GFM.
- (2) Rock properties, necessary to describe the flow of water through assigned lithofacies.
- (3) Geochemical sorption parameters that allow chemical species of interest to be tracked as they move through the lithofacies in the simulation domain.
- (4) A robust representation of subsurface heterogeneity. For the simulations presented, geostatistical variability in the lithofacies is included to show proof-of-concept and exercise the workflow.

All lithologic units below the Zefa Fm. to the base of the Menuha Fm. are given variability. The computational mesh is then assigned boundary conditions for both steady-state and transient flow

fields. Finally, hypothetical releases from waste disposal are simulated by releasing chemical tracers in the location of the proposed intermediate disposal borehole.

During the evolution of the project, the focus shifted from initially considering a subsurface geological repository for waste to our current emphasis on IBD disposal. Thus, the simulation domain for this report has shrunk to highlight flow and transport in a localized region surrounding a single intermediate borehole. For this reason, the numerical representation of the intermediate borehole disposal is limited to 100 m x 100 m laterally, and ranges stratigraphically from the base of the Hazeva Gr./ Zefa Fm. conglomerate through the base of the Judea Gr./ Nezer Fm. limestone for a total depth of 160 m (Bussod *et al.*, 2020). The borehole is represented as a column of nodes located at the center of the domain, each 4 m³ (2m x 2m), and running from an elevation of 300 m down to 200 m. The IBD borehole thus has a total volume of 400 m³ in our simulations. This simplified representation of a disposal borehole can easily be modified to account for more details as the borehole disposal design advances.

3.3 Update of Initial Subsurface Water Saturation Conditions

Using the updated FY21 GFM and new NRCN and GSI infiltration values for the Negev desert region from the analysis of near surface borehole data and literature paleoclimate data (2017-2020 Final Report, Section 3.2; Bussod *et al.*, 2020), we re-evaluated the subsurface water saturation conditions for the Yamin Plain, Northeastern Negev desert.

3.3.1 Steady-State Saturation Background Simulations

The background, long-term steady state flow field (referred to as the ‘base case’) for the Yamin Plain is based on our understanding of infiltration in desert regions of the southwestern United States. Infiltration fluxes based on estimates from Yucca Flat, Nevada (Kwicklis *et al.*, 2006) and the Pajarito Plateau (Birdsell *et al.*, 2005) where detailed chloride and stable isotope signals have been used to constrain infiltration fluxes. For undisturbed sites with native vegetation, steady-state fluxes have been estimated for these areas to be on the order of less than 1 liter per square meter per year (1 mm/y). In fact, the Yucca Flat analysis revealed negative infiltration, with the strong suction of the root zone pulling water from depth over an estimated 6000+ years (Kwicklis *et al.*, 2007). In the absence of such detailed chloride and stable isotope data from the Yamin Plain, and with some early estimates of present-day infiltration for the Negev desert in the Yamin Plain area, we chose to arbitrarily fix the base case for infiltration to 0.1 mm/y (0.1 L/m² per year).

After creating new property distributions from the updated data collected by our Israeli colleagues, we created a background run to be the base saturation profile for climate change, heat, and transfer runs. In order to set up present-day initial conditions, the site model was first fully saturated to simulate wetter regional Glacial Period conditions that ended between 8,000 and 10,000 years ago and simulated a post-Glacial arid environment using a 0.1 mm/y infiltration flux from 10,000 years to present allowing the excess water to drain out of the bottom of the domain gravitationally. The

bottom of the domain was assigned a fully saturated condition to facilitate flow out of the domain and at 10,000 years the model saturation reached steady-state and the present-day saturation profile approximation was produced (**Figure 3-5**).

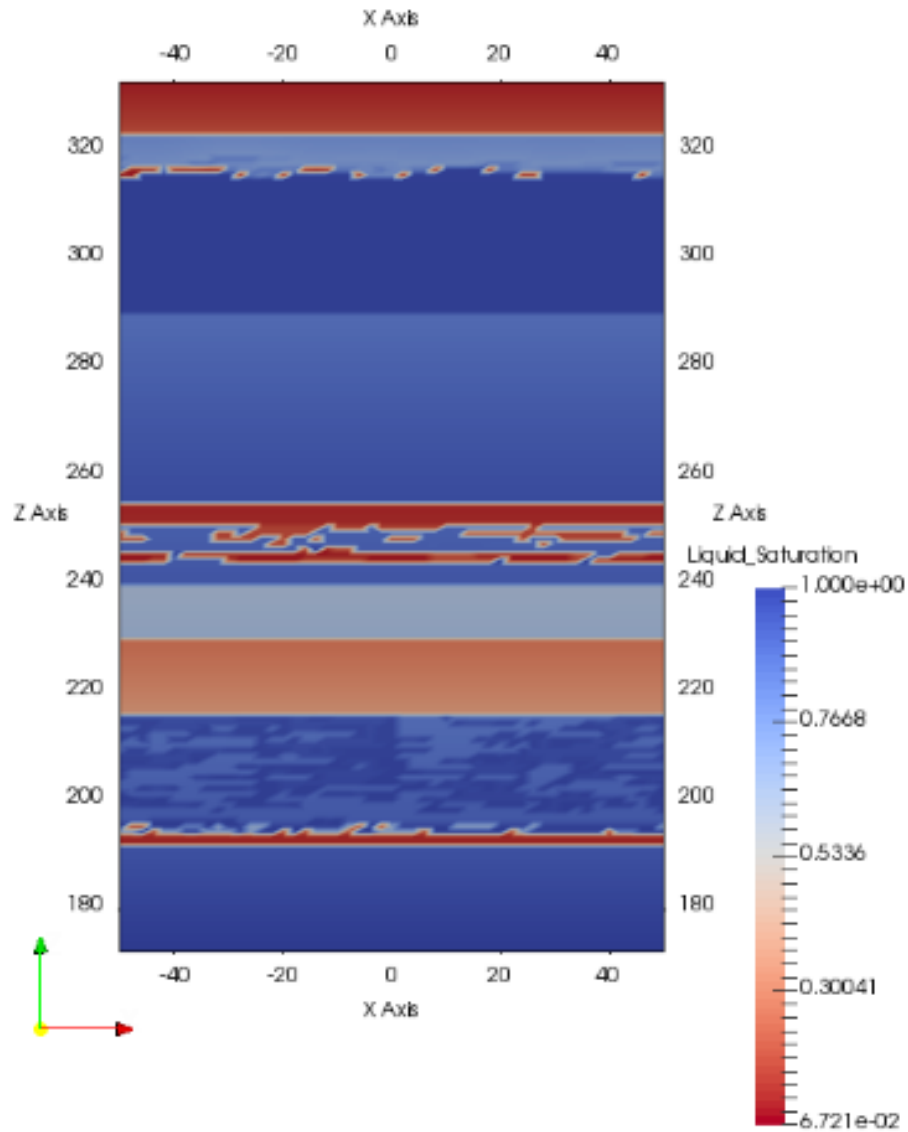


Figure 3-4. 2D Slice of 3D present-day model of initial Negev subsurface liquid saturation state. High saturation is shown in blue and low saturation is red.

Using the previous results of a 1D model of the Negev subsurface (Bussod *et al.*, 2020 - blue curve) and the results above (**Figure 3-5**), we can evaluate the saturation profile of the heterogeneous model (**Figure 3-6**, grey curve)Error! Reference source not found.. Generally, we see that the saturation profile is quite close to the 1D results and to measured Negev borehole data (red asterix).

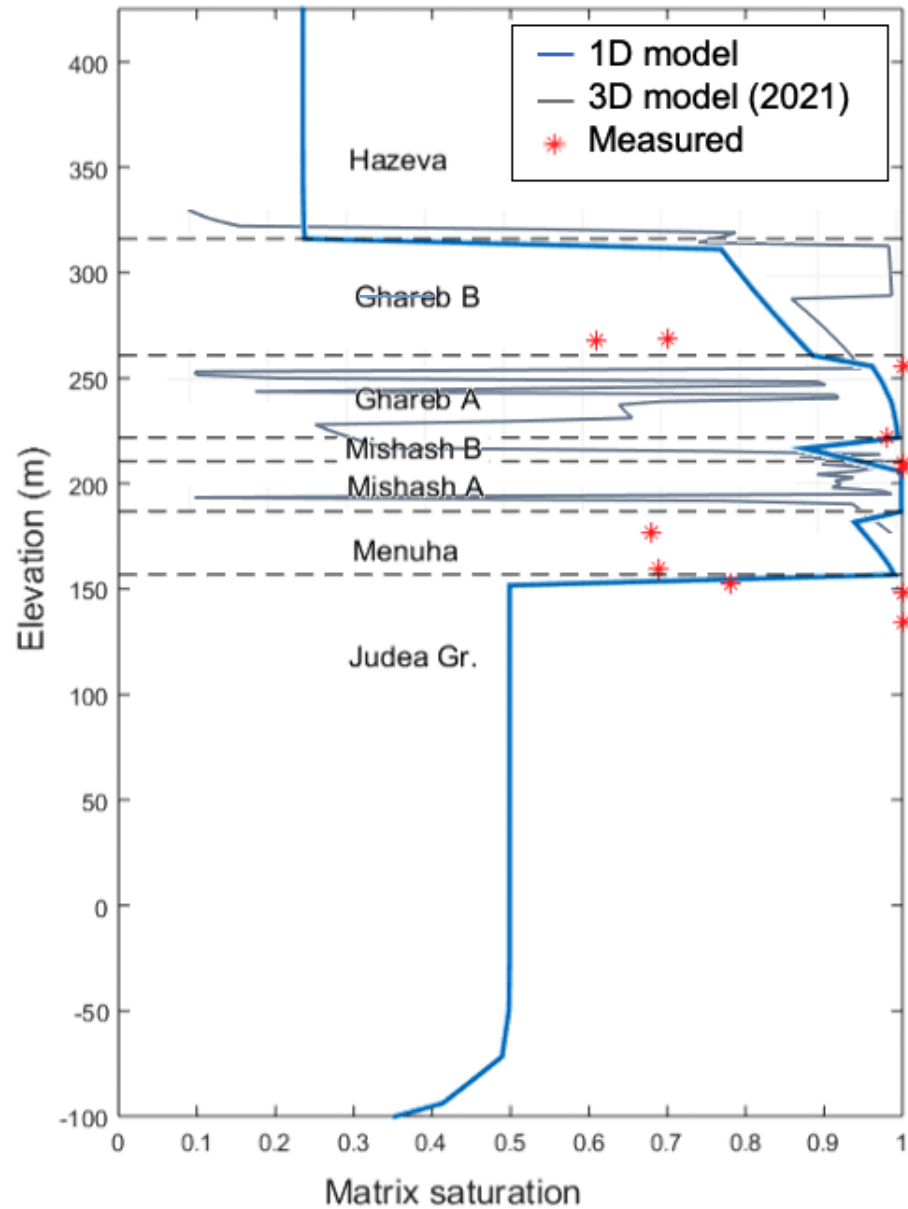


Figure 3-5. Saturation profile along the vertical z-axis of the IBD for the 3D heterogeneous property distribution model (gray line) versus the saturation profile of the 1D model (blue line) and field saturation data from Negev desert wells (red asterix).

HFUs with relatively low saturation are due to the heterogeneous distribution of lower-permeability materials in generally high-permeability layers. This new saturation profile shows that the new model results in a wetter initial present-day saturation condition than earlier models for the Ghareb-B HFU and generally comparable for the other HFUs but with greater variability.

3.4 Flow and Transport Models

For our FY21 simulations we use the new 3D saturation condition in **Figure 3-5** as our initial state for flow and transport simulations. In these simulations we use both FEHM and PFLOTRAN codes to evaluate the effects of heat-generating waste packages in the Yamin Plain subsurface around the IBD. The computational domain for the thermal loading simulations is shown in **Figure 3-6**.

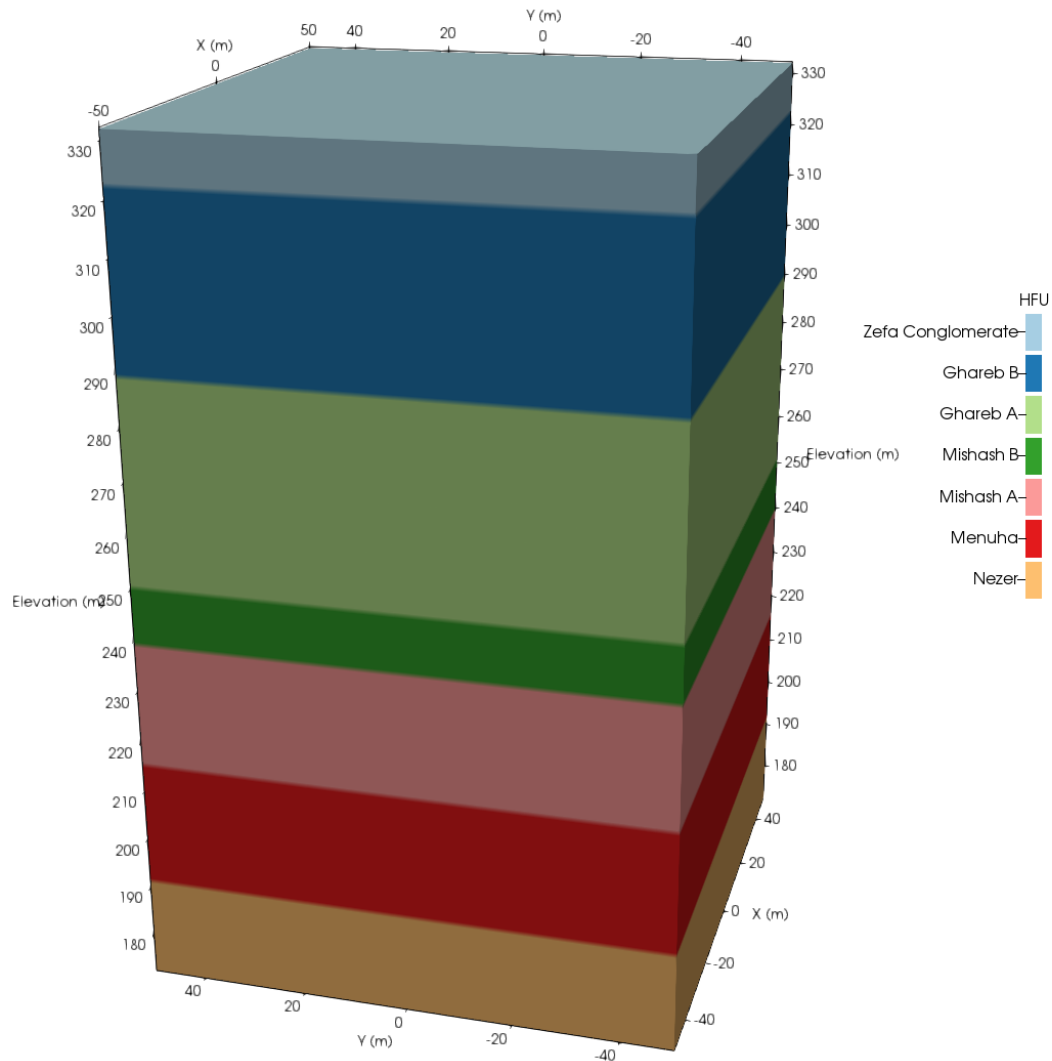


Figure 3-6. 3-D Computational IWD Domain (100m² x 160m) with Seven Hydrofacies Units (HFUs).

In the absence of specific or new data, we used thermal loading values for *Used Fuel* waste derived from the literature (Carter *et al.*, 2012) and rock thermal conductivity values measured on Negev carbonate lithologies by Sandia National Lab and GSI colleagues a (Bauer *et al.*, 2021; Itay Reznik, GSI, *pers. Comm.*, 2021). This work encompasses modeling the time- and temperature-dependent evolution of subsurface physical properties (e.g., saturation and temperature) due to thermal loading in the nearfield region of the intermediate borehole depth (IBD) location.

3.4.1 Ponding Climate Scenario Runs

In addition to our FY20 climate simulations one of the additional climate conditions we tested was a cyclic ponding condition. **Figure 3-7** shows the “top” of the modeled domain of the Negev subsurface (the top of the domain is at 332 m elevation – the true surface is above 400 m elevation). The cells colored dark red are assigned the ponding boundary condition. The increased ponding we chose to test was to apply 40,000 kg/day of water infiltration every 50 years for 50 days to the cells colored red. After the first ponding cycle completes (at 50 days), the top twenty meters are saturated more fully, and by the time the final ponding cycle completes (after 50 days, and 150 years), the top 100 m experiences an increase in liquid saturation (c.f., **Figure 3-8**). At this point, much of the pond water has yet to disperse horizontally throughout the domain (**Figure 3-9**) and the flow and high saturation are focused under the ponding zone. By the end of the simulation, much of the water near the very top of the simulated domain has dispersed vertically and horizontally (**Figures 3-10 and 3-11**).

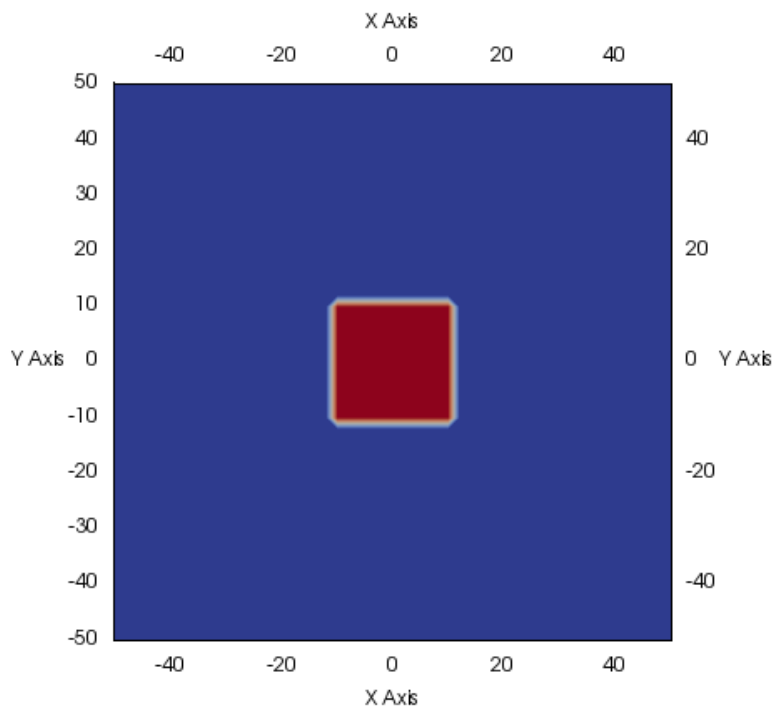


Figure 3-7. Top view of the ponding zone (50 m x 50 m) at Top of Hazeva Gr. alluvial sediments.

Two higher infiltration flux scenarios are implemented to explore possible climate change impacts that are hypothesized to result in increased infiltration fluxes of 30 mm/y and 210 mm/y. A final climate scenario involves repeated ponding at the IBD site. This is based on previous experience with ponding events at Los Alamos, NM (Stauffer *et al.*, 2005), caused by modifications to flow channels that led to standing water and rapid pulses of infiltration after heavy rains. We hypothesize that such ponding events can occur when climate induced variability in rainfall intensity and run-off leads to large pulse(s) that coincide with surface topography impacts at the site. For this scenario, we simulate repeated ponding that occurs during 5-day periods every 50 years. 400,000 kg of water are input for each pond, a value chosen based partly on the characteristics of alluvium and conglomerate, and their ability to accommodate a large transient water input over a short time period. This value is comparable to mass inputs from Stauffer *et al.* (2005) at the Los Alamos Canyon weir site, which is an example of how changes to surface topography can lead to short bursts of high-intensity infiltration.

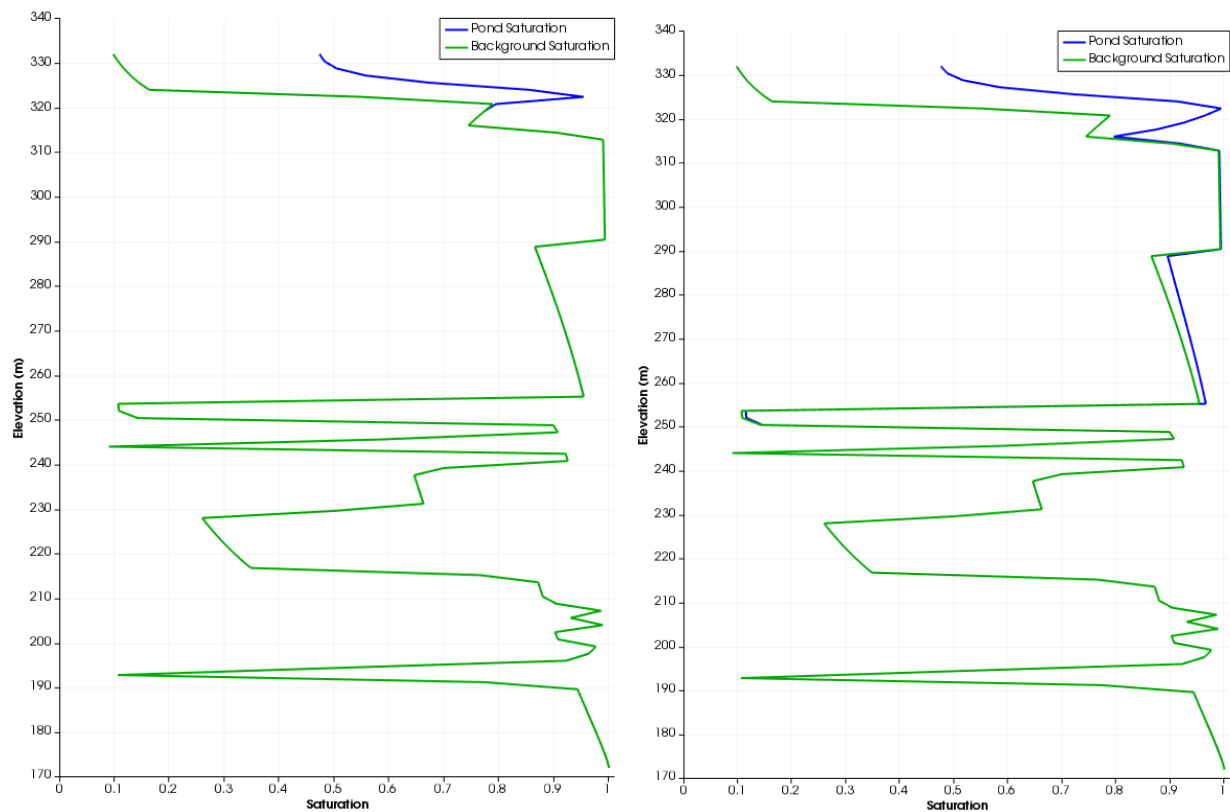


Figure 3-8. Saturation profile along z-axis at $x = 0$ m, $y = 0$ m for background and ponding at 50 days (left), and 150 years (right).

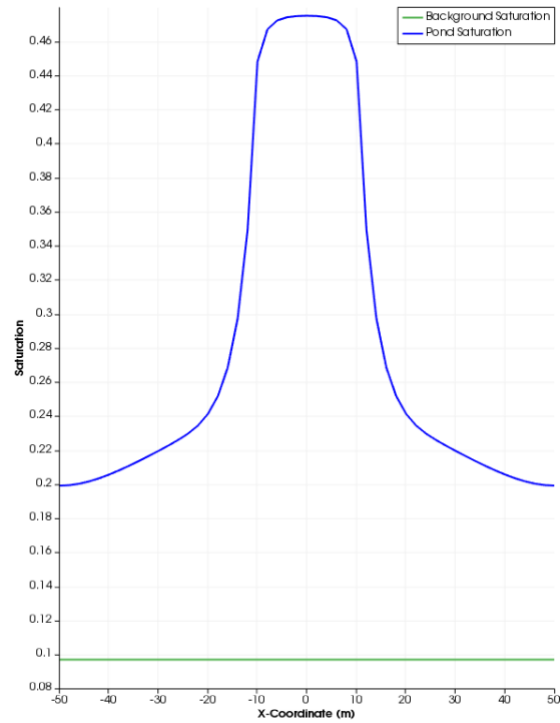


Figure 3-9. Saturation profile along x-axis at $y = 0$ m, $z = 332$ m for background and pond at 150 years.

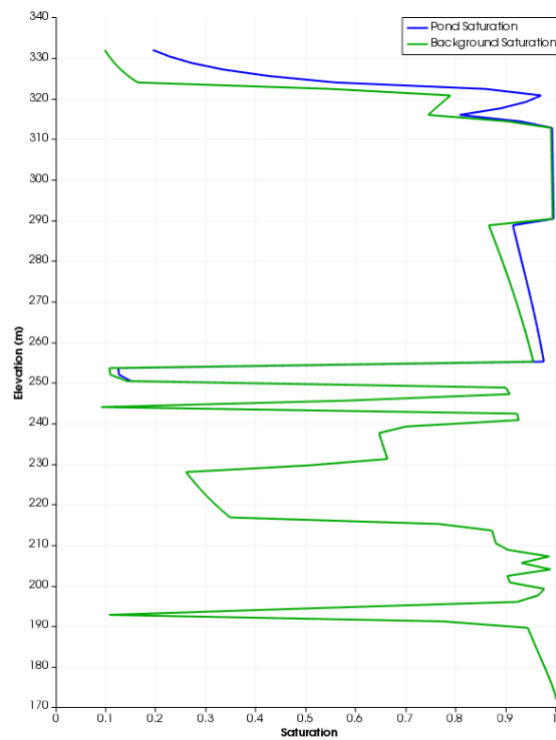


Figure 3-10. Saturation profile along z-axis at $x = 0$ m, $y = 0$ m for background and pond at 200 y.

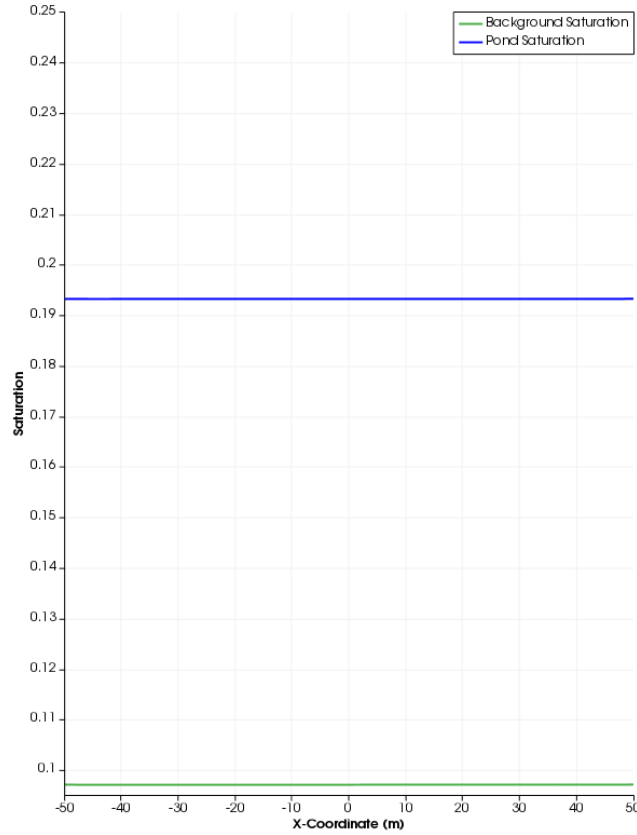


Figure 3-11. Saturation profile along x-axis at $y = 0$, $z = 332$ for background and pond at 200 y.

3.4.2 Ponding Infiltration Footprint

Because the top of the simulation domain is not at the land surface, simulations of flow through Hazeva Gr. alluvial deposits, from the land surface to the top of our IBD computation domain (Zefa Fm. conglomerate) were performed to determine the amount of lateral spreading during flow through the alluvium. **Figure 3-7** shows the location of the infiltration region at the top of the Hazeva Gr. as the red square patch. The top of the IBD model is located 140 m below the surface based on Y-16 data. There is potential for horizontal spreading of any infiltration introduced at the surface, however we show in Bussod *et al.* (2020) that there is minimal horizontal spreading, but rather the water travels as a fast pulse from the surface pond to the top of the conglomerate. This result leads us to conclude that given the dimensions of our IBD model, to a first approximation, a 50 m x 50 m surface pond geometry at the desert surface can be represented as an equally sized patch at the surface of the Ghareb Fm. conglomerate that is the top boundary of our IBD computational mesh. Here we note that the Hazeva Gr. sediments extending from the land surface to the Zefa Fm. conglomerate contain not only alluvium but also clay lenses that could cause horizontal spreading. In the future, a separate investigation using geostatistics could be done to characterize variations in the clay distributions and resulting horizontal spreading of an infiltration front.

3.5 Flow and Transport Simulation Results

Results for the migration of water through the IBD simulation domain from the top of the Ghareb Fm. to the Base of the Nezer Fm. are presented in this section. All transient scenarios begin from a background ‘base case’ infiltration rate of 0.1 mm/y. Saturation is defined as the fraction of pore space filled with water, such that a saturation of 1.0 means that the porosity contains only water.

3.5.1 Reactive Tracer Simulations Update

Progress was made on simulating a reactive tracer with sorption properties included for the different HFUs from 2017-2020 Final Report, 2020 (**Table 3-3**; Bussod *et al.*, 2020) to observed how a tracer may migrate through the subsurface under wetter conditions. The reactive tracer chosen for the simulations is ^{235}U . During the simulation, ^{235}U was continuously introduced into the nodes in the borehole (at $x = 0$ m, $y = 0$ m, and $z = 200$ to 300 m elevation) at a concentration of $1 \text{ mol } ^{235}\text{U}/\text{m}^3$ and an inflow rate of $1\text{e}^{-20} \text{ kg/y}$. This results in a total injection of $1\text{e}^{-14} \text{ mol}$ of total ^{235}U over the 1,000 year simulation.

Table 3-3. Summary of Hydrologic Properties for Negev Samples HOP-5, CK-6, LS-12, CL-8, SS-10 (from 2017-2020 Final Report, (Bussod *et al.*, 2020). Saturated hydraulic conductivity (K_{sat}) was measured using *Falling-Head Rising-Tail Flexible Wall* method (Bussod *et al.*, 2020, Appendix A). van Genuchten parameters for unsaturated samples were calculated using the RETC code (van Genuchten *et al.*, 1991) to fit the measured moisture retention points and characteristic curves for hydraulic functions (i.e., relative permeability and capillary pressure).

Sample Number	Lithology	K_{sat} (cm/sec)	α (dimensionless)	n (%vol)	θ_r (%vol)	θ_s (%vol)
HOP-5	Phosphorite	3.30E-05	0.0006	1.3976	0	0.4
CK-6	Chalk	6.80E-08	0.0001	1.591	0	0.21
LS-12	Limestone	1.10E-08	0.0003	1.2534	0	0.13
CL-8	Clay	5.30E-09	0.0002	1.316	0	0.35
SS-10	Sandstone	2.30E-04	0.0051	1.7103	0.02	0.14

The behavior of the tracer was tested for four different scenarios:

- (1) A ponding scenario where 40,000 kg of water was applied at the top ponding zone for one day at the start of the simulation.
- (2) A low, background infiltration rate of 0.1 mm/y applied at the ground surface.
- (3) A medium infiltration rate of 30 mm/y.
- (4) A high infiltration rate of 210 mm/y.

Figure 3-12 shows the results after 100 years of simulation time of the four scenarios. After 100 years, the ^{235}U has not migrated far from the borehole, showing that the adsorption to the HFUs does have a strong control on the extent of contaminant migration. Though the difference between the infiltration scenarios does not show a strong sensitivity of the tracer migration to the boundary conditions at the top, there are some subtle differences in the concentrations at the periphery of the different plumes, suggesting the higher infiltration allows for faster mixing.

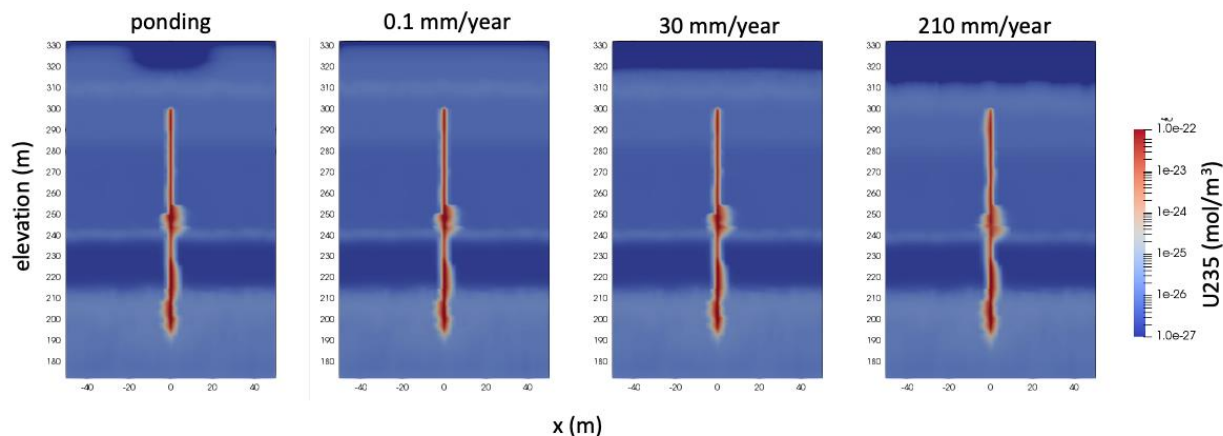


Figure 3-12. Total dissolved uranium for four infiltration scenarios after 100 years.

Figure 3-13 shows the ^{235}U tracer migration at four snapshots in time from a continuous contaminant source. The tracer is much more mobile in the Nezer Fm. compared to the overlying layers, suggesting that near surface contamination is not of as great of concern, assuming the Nezer properties are homogeneously distributed. Additional simulations are needed with higher concentrations of ^{235}U in addition to non-continuous ^{235}U sources to observe transport behavior. These results demonstrate that given current properties, in the case of a continuous source, it is likely for uranium migration to occur below the Nezer Fm., however, this work is ongoing and further testing and potential scenarios will be considered.

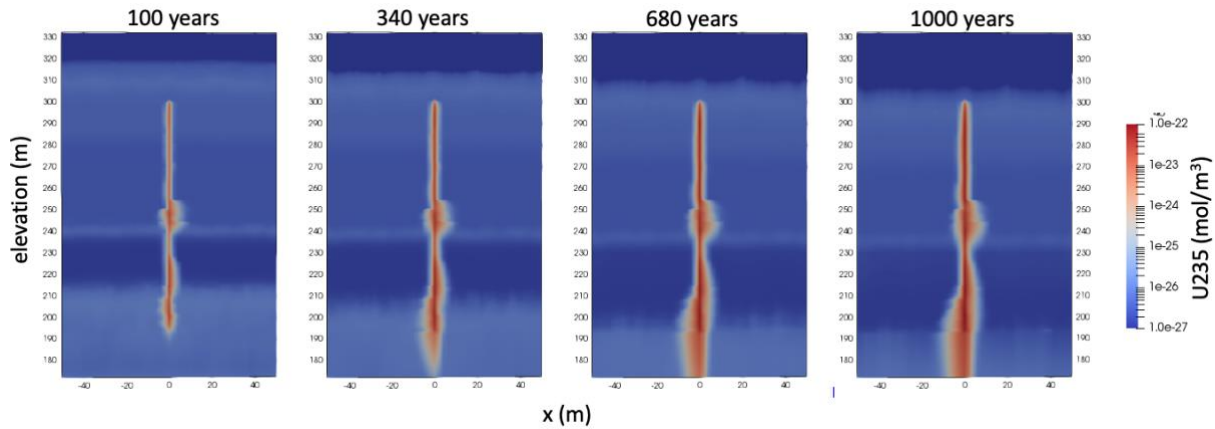


Figure 3-13. Dissolved ^{235}U tracer migration for 30 mm/y infiltration scenario through time.

3.6 Heat-generating Radionuclide Waste Simulations

We further developed the FEHM and PFLOTRAN models to evaluate the effects of heat-generating waste in the subsurface. For these simulations, an energy source was distributed equally throughout the borehole (at $x = 0$, $y = 0$, from $z = 200$ m to $z = 300$ m). The IBD is thus $4 \text{ m}^2 \times 100 \text{ m}$ long with a total volume of 400 m^3 having the same volume as a cylindrical borehole with a radius of 1.13 m. The heat-generation is introduced into the borehole in three ways: first, we use a flat, 12 kW energy source for the first 20 years; second, we use a 12 kW energy source with a 30-year half-life to represent radioactive decay. Third, we use a calculated decay heat function for 40 GWd per metric ton (GWd/mT) reactor fuel that has been allowed to sit at the surface for 30 years based on data from Carter *et al.* (2012). In this case, the initial thermal load at time zero in our simulations would require 13.2 tons of waste generating 910 W per ton. For the heat decay function, we use a step-linear approximation that is plotted against a standard 30 year half-life decay in **Figure 3-14**. The step-linear function in FEHM has breakpoints at 0, 20, 40, 70, 270, and 470 years. Additionally, we also assign to the entire top boundary a constant 20°C and to the entire bottom boundary a constant 23°C . Lateral boundaries are no-flow with respect to heat.

During code testing, we initially ran simulations comparing a constant thermal load to a simple 30 year half-life decay function, both starting at 12 kW total energy input. In the PFLOTRAN simulations, at 25 years (5 years after the flat energy source cuts off), the difference in temperatures produced by the flat versus 30 year half-life decay heat sources is substantial (**Figure 3-15**). For the 30 year half-life energy source, temperatures also reach temperatures above 100°C , particularly between 230 m and 290 m.

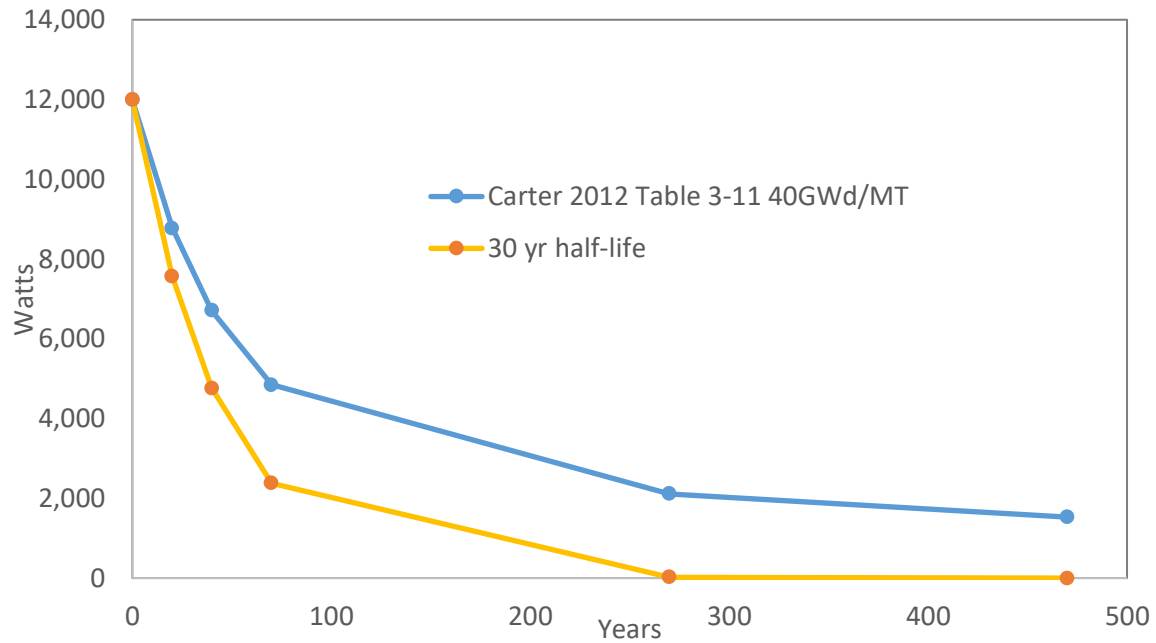


Figure 3-14. Step-linear energy source (blue) vs. half-life decay energy source (red).

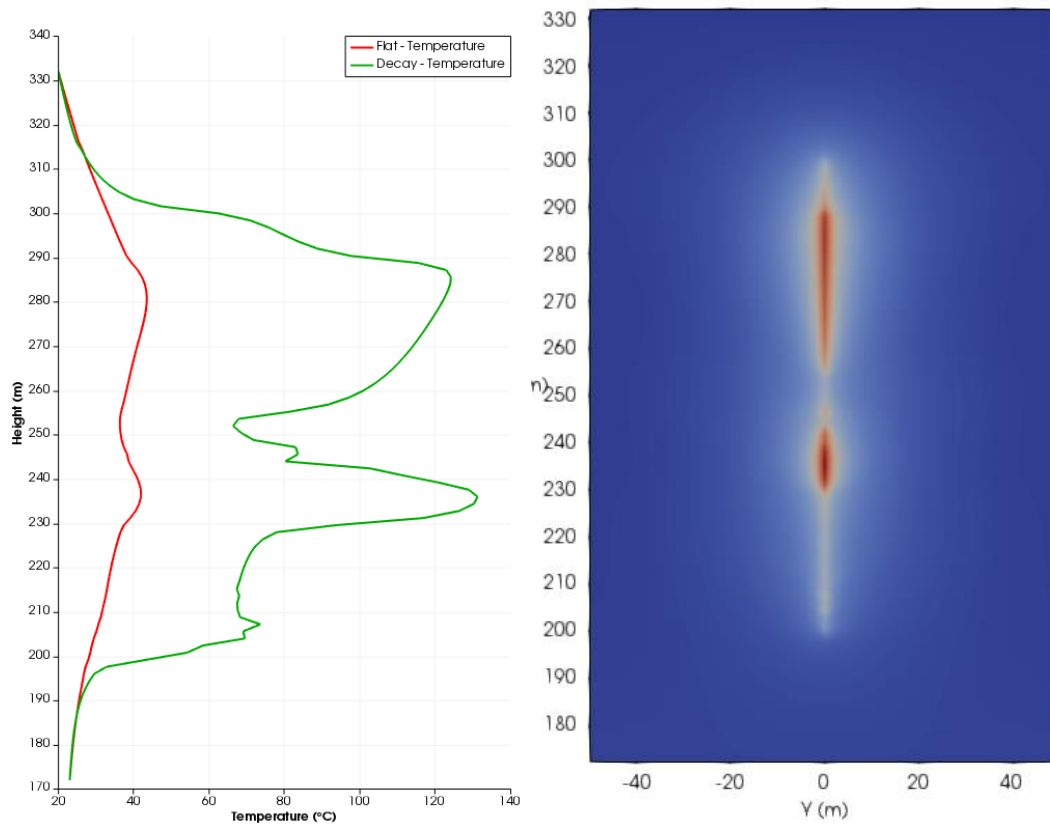


Figure 3-15. Temperature profile along z-axis at $x = 0$, $y = 0$ for both heat sources at 25 y (left), and plot showing temperature distribution across a slice of the model domain for the decaying heat source (right).

Notably, the temperature profile has substantial vertical variations, even between 200 m and 300 m (where the distributed source of energy boundary condition is applied). This variation in temperature coincides with the variation in both specific heat and thermal conductivity as a function of lithology. As in **Figure 3-16** and **Figure 3-17**, areas of particularly high temperature coincide with rocks that have a particularly low specific heat (e.g., depths of ~290 m to ~310 m), and low thermal conductivity. Low specific heat allows the rock to heat up very quickly, and a low thermal conductivity prevents the heat from dissipating into the surrounding rock.

By 200 years (**Figure 3-18**) the simulation with the flat heat source now has a linear temperature gradient from the top of the domain (20°C) to the bottom of the domain (23°C), and all excess heat has been dissipated and expelled from the system. The simulation with the 30 year half-life heat source still has peak temperatures at ~30°C.

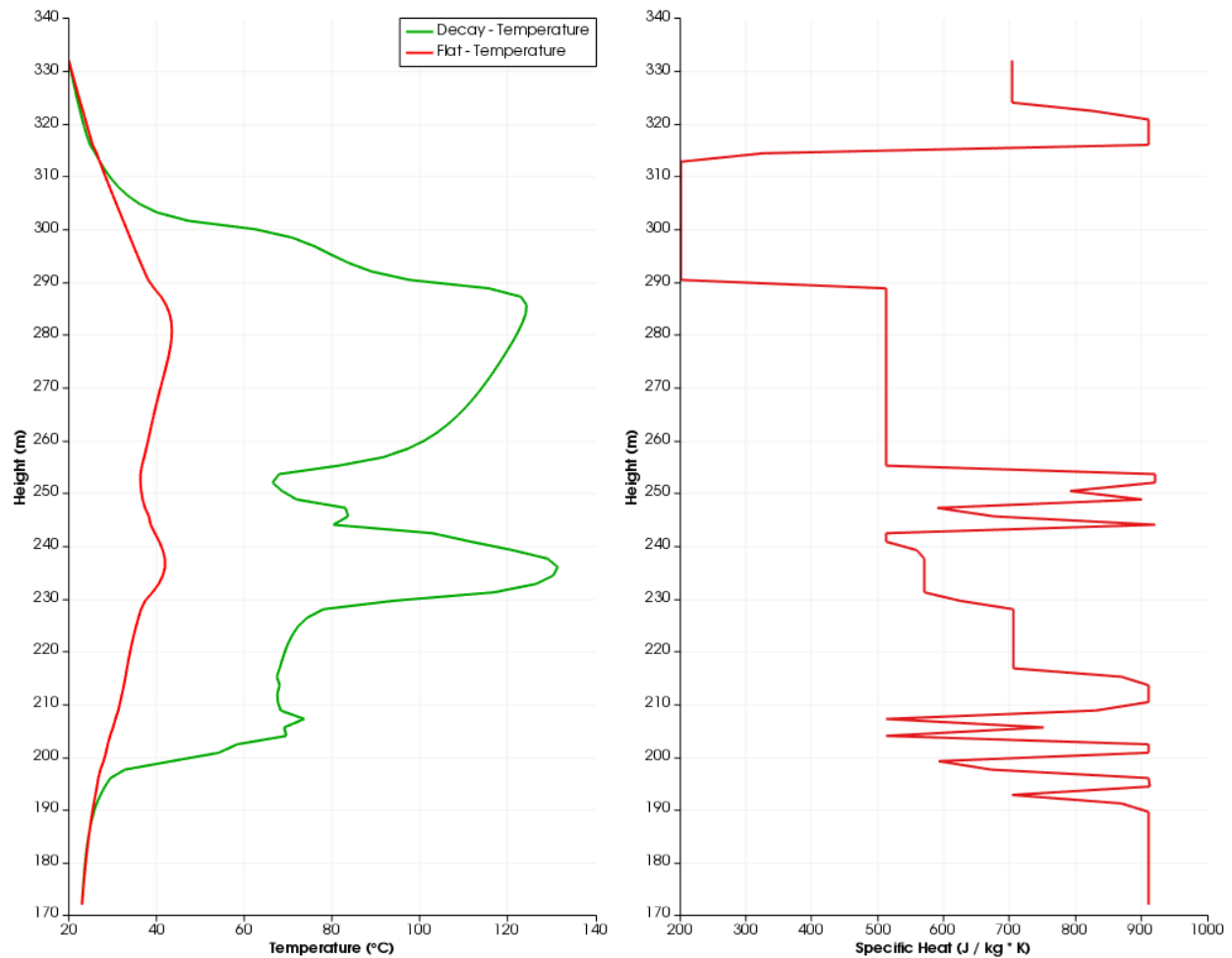


Figure 3-16. Temperature profile at 25 y (left) vs. the specific heat profile (right).

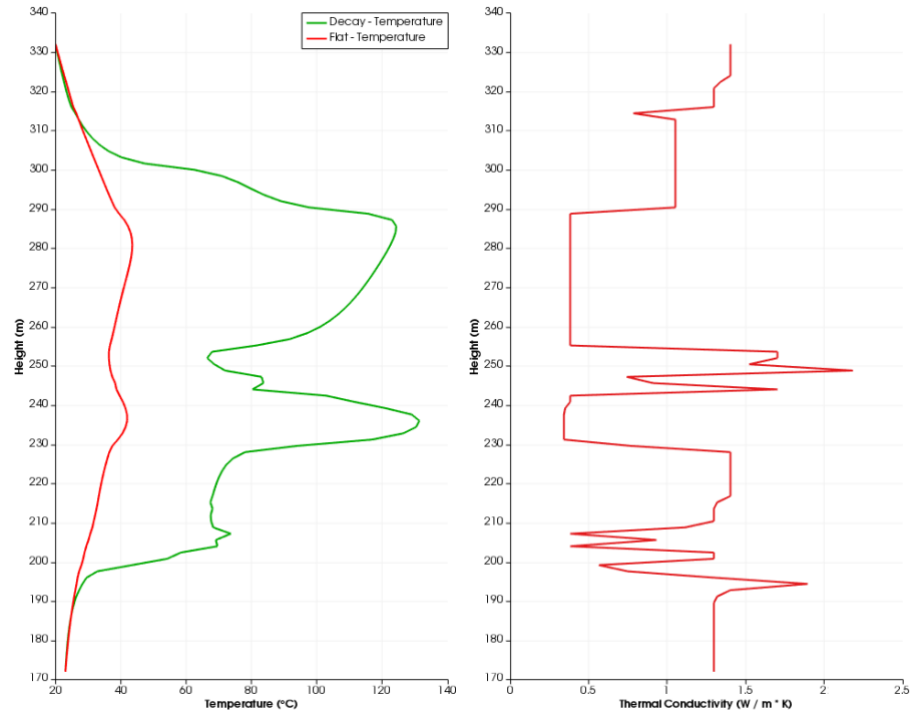


Figure 3-17. Temperature profile at 25 y (left) vs. the thermal conductivity profile (right).

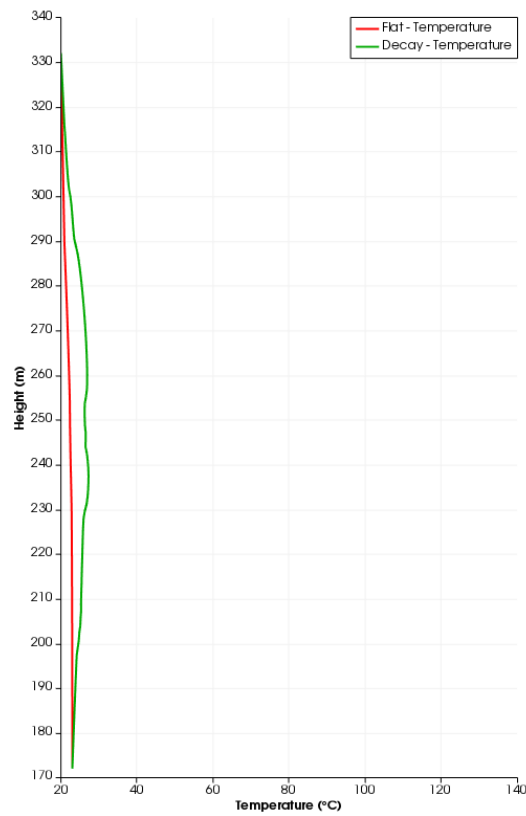


Figure 3-18. Temperature profile along z-axis at $x = 0$ m, $y = 0$ m for both heat sources at 200 y.

Figure 3-19 shows the results of the temperature profile of the nodes adjacent to the borehole after 5 and 50 years following the introduction of the decaying heat source. Results from both FEHM and PFLOTRAN are plotted, and we can see some disagreement between the two codes on the way heat convection is taking place around the borehole. The greater temperatures in the PFLOTRAN results may be the result of the way the borehole is currently being represented; the borehole nodes have the porosity reflecting the properties of the host HFU and not a 1.13 m radius cylindrical void filled with waste canisters and air. The FEHM model does, however, have the borehole explicitly defined with a porosity of 0.5, fixed heat capacity of 1000 W/(m.K), fixed density of 2000 kg/m³, and zero saturation. In the coming months we will develop the PFLOTRAN model to include the more complex waste borehole parameters.

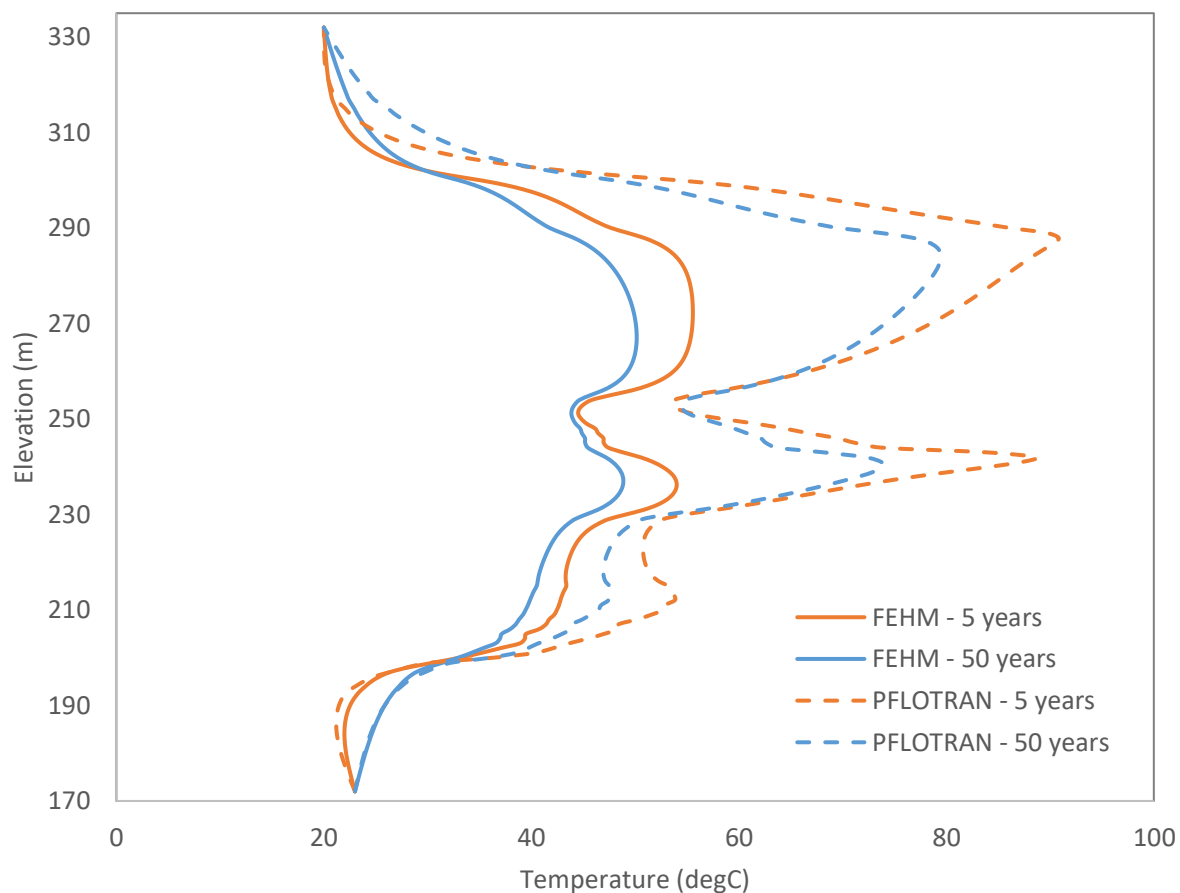


Figure 3-19. Results of the temperature of the nodes adjacent to the borehole ($x = 2$ m, $y = 0$ m) for the decaying heat source scenario for 5 and 50 years following source introduction.

Figure 3-20 and Figure 3-21 plot the saturation and temperature at selected elevations for the 40 GWd/mT decay heat case. The saturation response with elevation varies widely and is related to the hydrologic properties of the rocks adjacent to the disposal borehole. Locations near the center of the heated region show larger changes in saturation, with low initial saturations rising rapidly

in the 0.2 years (**Figure 3-22**) and then continuing to vary with time as moisture in the system is redistributed through vapor and liquid phase transport. At 228 m elevation, saturation initially at 70 % climbs at early time, then drops from 1 to 10 years before climbing again to over 90 % saturation after 60 years. These results are preliminary and we plan to further analyze the behavior of moisture around the disposal borehole in FY22.

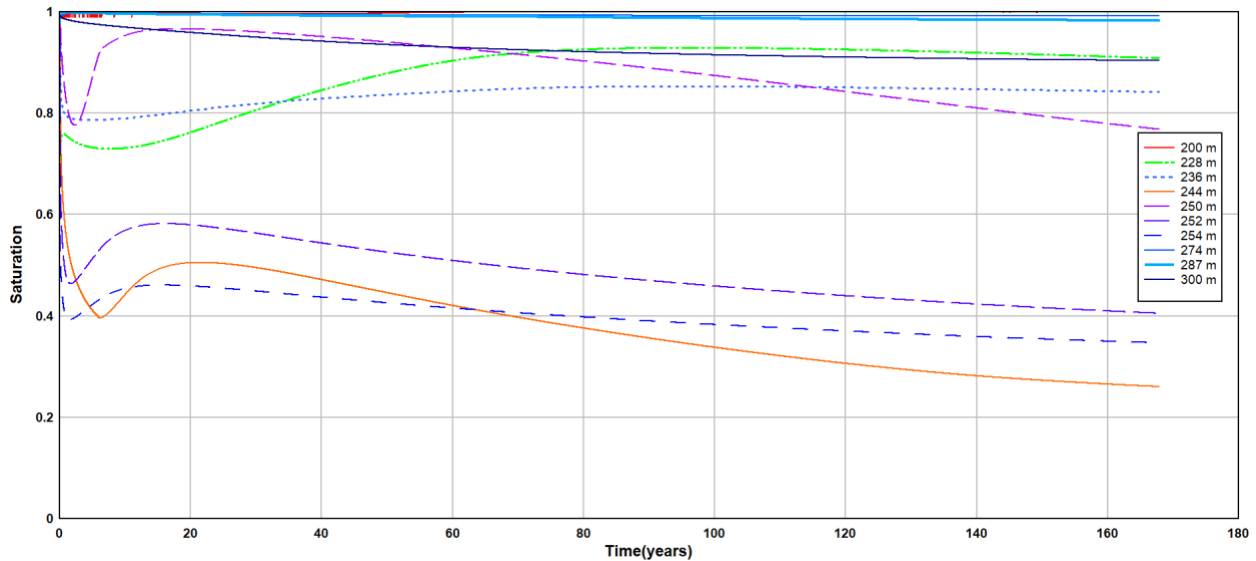


Figure 3-20. Saturation versus time on nodes adjacent to the borehole ($x = 2$ m, $y = 0$ m) for the 40 GWd/mT heat source.

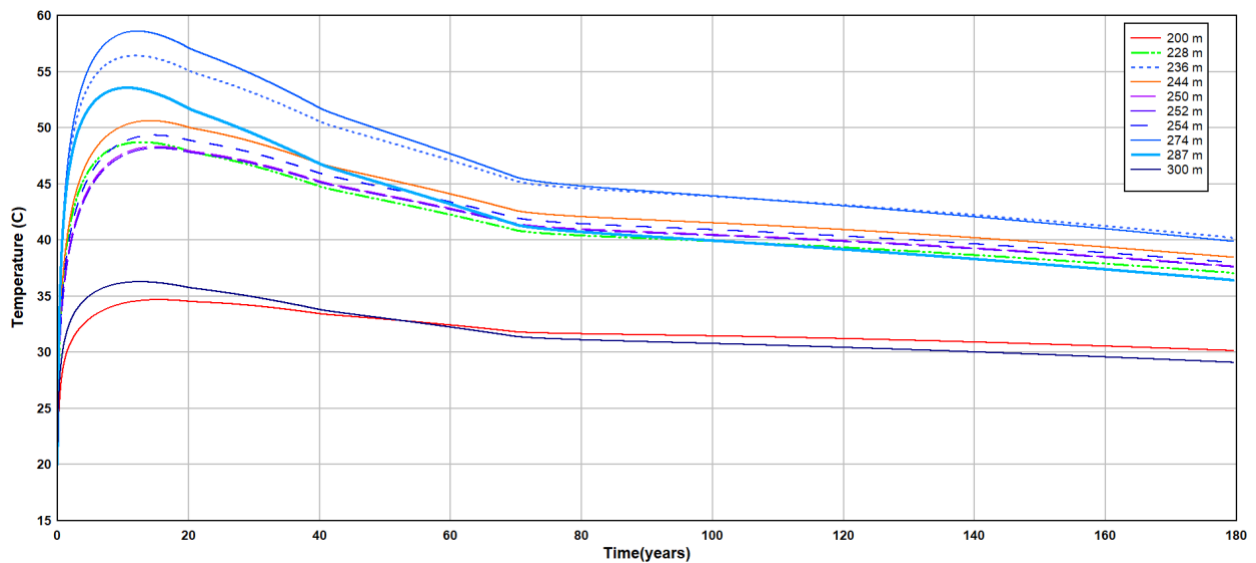


Figure 3-21. Temperature versus time on nodes adjacent to the borehole ($x = 2$ m, $y = 0$ m) for the 40 GWd/mT heat source.

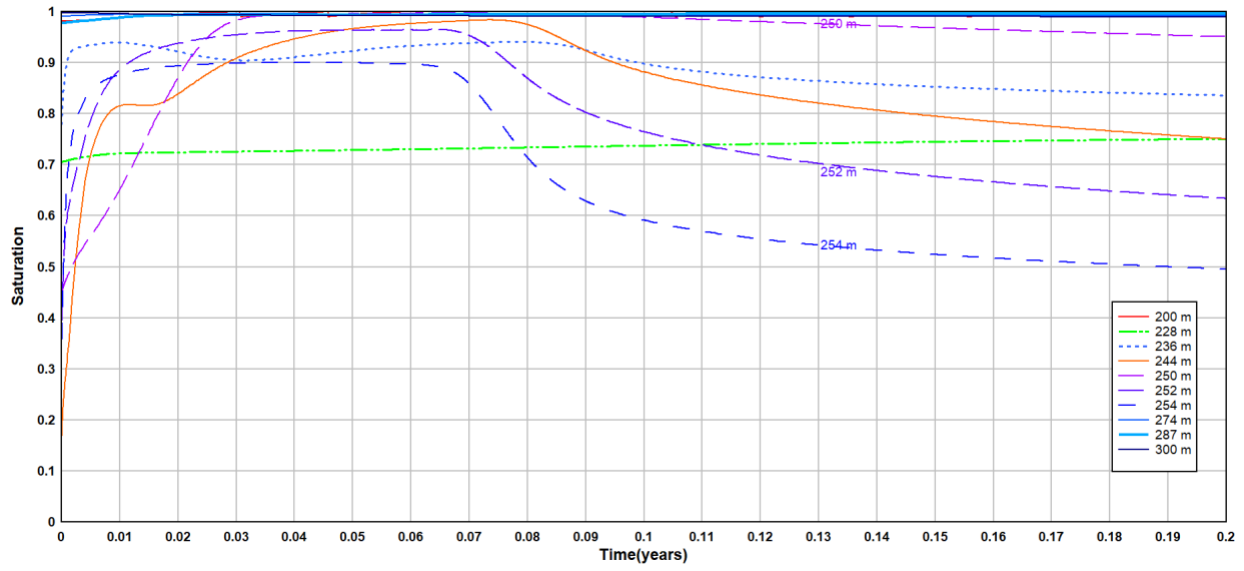


Figure 3-22. Saturation versus time to 0.2 years on nodes adjacent to the borehole ($x = 2$ m, $y = 0$ m) for the 40 GWd/mT heat source.

4 Experimental Geochemistry: Effects of Thermal Loading & Radiation on the Hydrogeochemical and Microstructural Evolution of the IBD Disposal of IAEC Nuclear Waste

4.1 Introduction

Prior to this year, the research from the LANL Geochemistry team was directed towards determining mechanisms for uranium sorption and kinetics in Negev carbonate rocks collected from desert outcrops and Yamin Plain borehole samples (Israel, 2017 and 2019). Even though this study was limited to uranium species, to a first approximation, we can use these results to provide insights into the potential migration of a radioactive contaminant plume originating from a subsurface disposal site. In FY20, we used our 2D and 3D F&T subsurface models in which experimentally-derived equilibrium Kd uranium sorption parameters and a uranium surface complexation model were implemented, to make preliminary predictions. In our 2017-2020 Final Report (Bussod *et al.*, 2020) we concluded that phosphate-rich and bituminous (organic-rich) Late Cretaceous, shallow marine lithologies located at IBDs within the Yamin Plain have a strong potential for providing an effective natural barrier to radionuclide migration.

In the 2021 the Geochemistry task for LANL, was re-focused on the issue of thermal loading associated with the emplacement of rad-waste packages in an IBD subsurface site. Specifically, to determine the effect of temperature on these key “natural barrier” organic-rich shallow marine lithologies. This new work directly addresses concerns related to the breakdown and remobilization of hydrocarbon phases (i.e., gas and liquid phases) in the vicinity of a subsurface nuclear waste borehole disposal facility, including:

- *The reaction chemistry and kinetics of thermal decomposition of bituminous (organic-rich) Negev carbonate rocks subjected to thermal loading from subsurface IBD waste disposal.*
- Determining the phase stability and thermally induced mineralogical phase changes affecting the modal mineral abundance and microstructural textures of organic-rich Negev lithologies.
- Measuring the types of chemical byproducts formed from bituminous Negev carbonate rocks during progressive heating up to 1100°C.

When completed, this study should also provide quantitative data on the effect of heating on microstructural changes in Negev rocks and their effect(s) on physical and chemical properties (e.g., porosity, permeability, hydraulic conductivity, actinide sorption capacity) of Negev

lithologies over time. This work will provide parameters and semi-empirical equations that can be input into our F&T process models.

4.2 Reaction Chemistry & Kinetics of the Thermal Decomposition of Organic-rich Negev Carbonates

Our FY21 geochemical, analytical and experimental activities were centered on characterizing the chemistry, microstructure, and kinetics of thermal decomposition of organic-rich Negev carbonate samples OS-2, OS-3, OS-4, HOP-5, OS-5.1, and OS-6.1. In this report however, we will not report on the characterization of samples OS-5.1 and OS-6.1 as they were only recently obtained from our Israeli colleagues at NRCN and their analysis is incomplete.

4.2.1 Source Materials

The samples investigated *represent* three bituminous carbonate marls (OS-2, OS-3, and OS-4) with respectively increasing organic carbon content of 9 wt.%, 11 wt.% and 15 wt.%, and a bituminous phosphorite (HOP-5) with a lower organic content (TOC = 1.61 wt.%). All of these samples are characteristic of the Late Cretaceous shallow marine rocks present in the Yamin Plain subsurface in the vicinity of the proposed IBD waste disposal site, Northeastern Negev desert, Israel. Details of their mineralogy, microstructure and composition can be obtained in the 2017-2020 NNSA Final Report (Bussod *et al.*, 2020).

4.2.2 Analytical Methods

Sample characterization and results from thermal decomposition and reaction kinetics analyses are measured using *X-ray fluorescence* (XRF) and *X-ray diffraction* (XRD) measurements for compositional and model mineral abundances. For quantifying thermally-induced microstructural and mineralogical phase changes and reaction kinetics we use (i) *thermogravimetric analysis* and *differential scanning calorimetry* (TG-DSC) from ambient temperature to 1100°C at different heating rates, (ii) *in-situ X-ray diffraction* (*in-situ* XRD) as a function of temperature, and (iii) *in-situ diffuse reflectance infrared Fourier transform spectroscopy* (*in-situ* DRIFTS) as a function of temperature.

We are also performing extensive characterizations of the pore structure of the samples using *nano-computed tomography* (nano-CT), but the data is being processed and will be presented in subsequent FY22 reports.

We have also initiated thermal aging studies at 200°C that are also not be presented in this report. These studies consist of incubating samples in sealed Parr autoclaves at 200°C in individual autoclaves that are collected after one, three, six, and twelve months for characterization. For each rock type, we prepared a set of autoclaves under both aerobic anaerobic (argon) conditions. Data from these studies will constitute a baseline characterization that will complement similar studies

on samples planned for FY22 that will undergo irradiation at different radiation levels. Once completed, data from the characterized samples will be used to accurately assess the performance of the organic-rich Negev lithofacies as potential hosts for an IBD spent nuclear waste disposal system.

4.2.3 Sample Characterization

To investigate the composition of the rock samples used in this study, we performed (i) X-ray fluorescence (XRF) and quantitative powder X-ray diffraction (qXRD) to determine the identity and modal mineralogy of the crystalline phases, and (ii) thermal and mass-spectroscopy elemental analysis techniques to measure the total organic carbon content (TOC) and adsorbed water of the samples. Graphical presentation and statistical information of the refinements are presented in **Figures 4-1, 4-2, 4-3, and 4-4**.

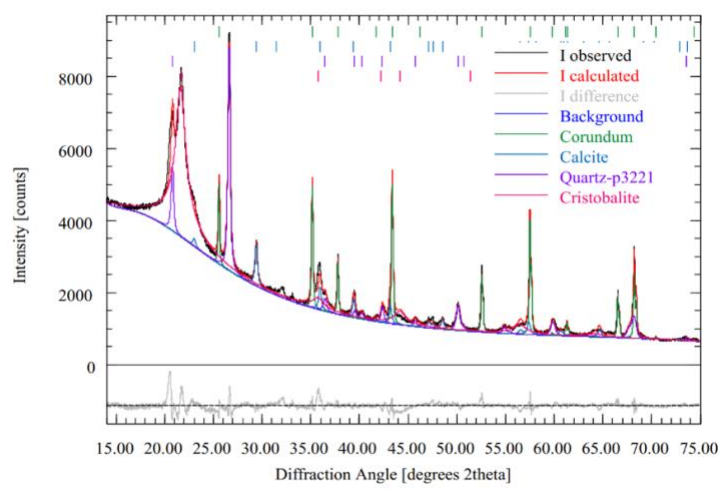


Figure 4-1. Quantitative X-ray diffraction refinement of OS-2. Corundum content of 20 wt.% added. Refinement parameters: $R_{wp} = 4.11$, $R_{exp} = 2.19$, $X^2 = 3.52$, $GoF = 1.88$.

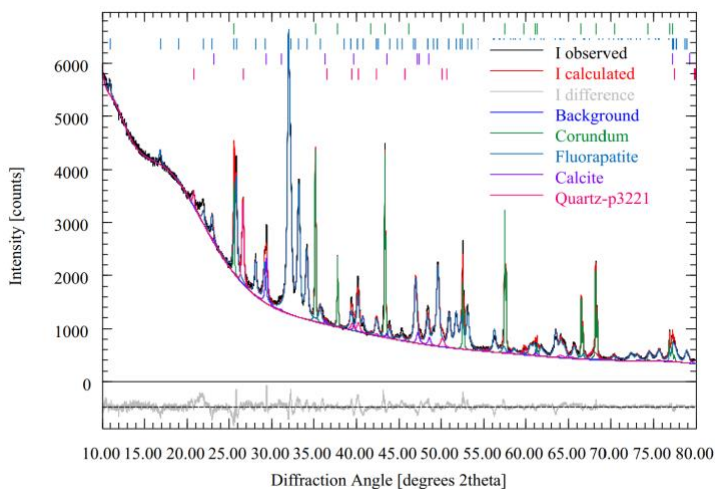


Figure 4-2. Quantitative X-ray diffraction refinement of OS-3. Corundum content of 20 wt.% added. Refinement parameters: $R_{wp} = 3.51$, $R_{exp} = 2.42$, $X^2 = 2.10$, $GoF = 1.45$.

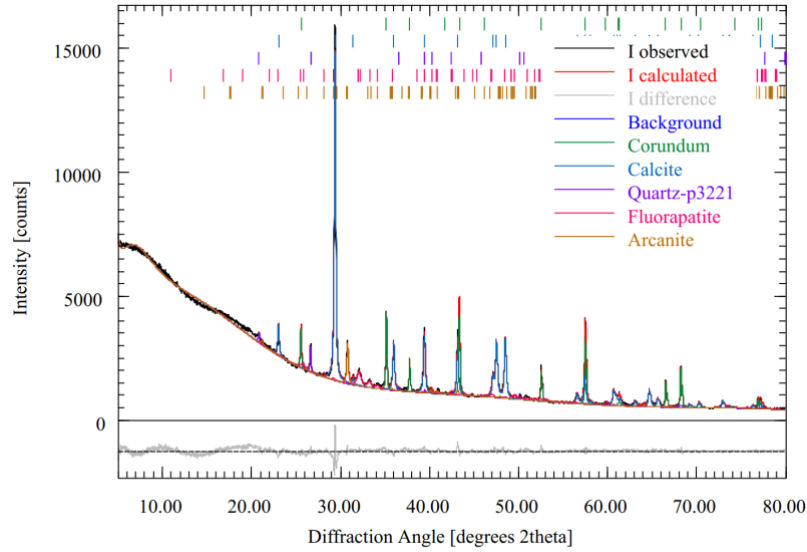


Figure 4-3. Quantitative X-ray diffraction refinement of OS-4. Corundum content of 20 wt.%. Refinement parameters: $R_{wp} = 3.17$, $R_{exp} = 2.19$, $X^2 = 2.10$, GoF = 1.45.

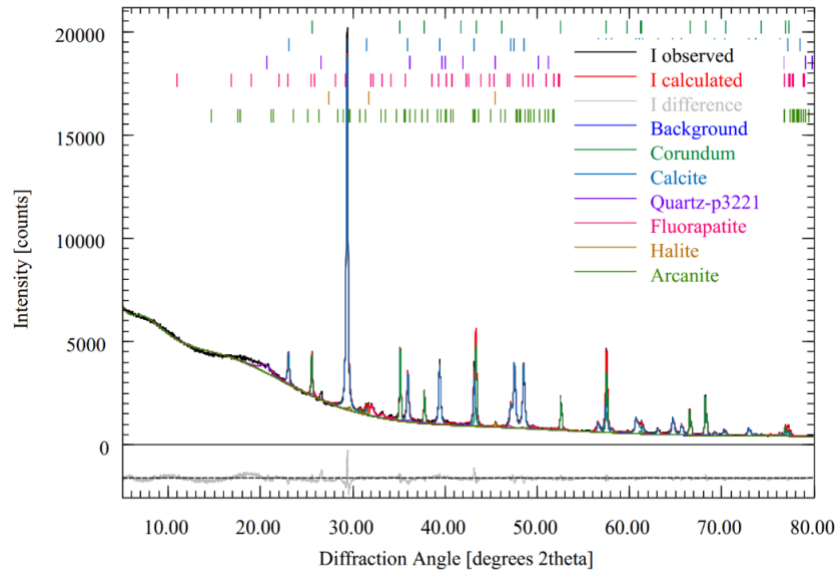


Figure 4-4. Quantitative X-ray diffraction refinement of HOP-5. Corundum content of 20 wt.% added. Refinement parameters: $R_{wp} = 3.26$, $R_{exp} = 2.22$, $X^2 = 2.16$, GoF = 1.47.

Results for the calculated mineral phase abundances (wt.%), total organic carbon content (TOC, wt.%) and adsorbed water measured by thermogravimetric analysis (TG) and elemental mass spectrometry (EMS) for each sample are shown in **Table 4-1**.

From the four samples investigated in this study, we have determined that:

- (1) The two bituminous carbonate marls, OS-3 and OS-4, are richest in TOC (12-15 wt.%) and calcite (53-54 wt.%) and possibly clay (OS-3: ~17 wt.%; Table 4-2, Bussod *et al.*, 2020).
- (2) Sample OS-2 is a silica-rich bituminous marl containing a large amount of an amorphous inorganic phase(s), possibly volcanic glass and/or clay (48 wt.%), as well as a-quartz (18 wt.%), cristobalite (15 wt.%) and a moderate TOC content (~9 wt.%).
- (3) Sample HOP-5 is an organic-rich fossiliferous phosphorite with over 65 wt.% carbonated calcium fluorapatite and approximately 2 wt.% TOC.
- (4) Adsorbed “free” water content for all samples is low (~2 wt.%).

Table 4-1. Inorganic and Organic Phase Contents of Negev Samples. Determined from quantitative X-ray diffraction (qXRD), thermogravimetric analysis (TG), and total organic carbon (TOC) measurements.

Sample	Arcanite	Calcite	Cristobalite	Fluorapatite	Halite	Quartz	Amorphous Inorganics	Organics	Water	Total
OS-2		9%	15%			18%	48%	9%	2%	100%
OS-3	2%	54%		8%		3%	18%	12%	2%	100%
OS-4	2%	53%		5%	0.5%	2%	20%	15%	2%	100%
HOP-5		4%		65%		7%	21%	2%	2%	100%

Combined with SEM imaging and mass spectroscopy elemental analyses (Bussod *et al.*, 2020), we conclude that the combination of multiple analytical techniques allows us to better characterize and understand the effects of thermal loading on different Negev lithologies. In FY22 we will be revising this analysis to consider clay and other minor phases that have not been included in this preliminary report.

4.2.4 Reaction Chemistry & Kinetics of Thermal Decomposition for Bituminous (organic-rich) Negev Carbonate Rocks.

In order to investigate the sensitivity of bituminous Negev carbonates subjected to thermal loading from subsurface IBD waste we use the analytical techniques and methods of thermogravimetric (TG) analysis, differential scanning calorimetry (DSC), and mass spectrometry (MS) to quantify the thermal behavior of both inorganic and organic phases present in the rocks. The experiments were conducted in argon, an inert environment mimicking pyrolysis conditions. Results from the TG and derivative TG (DTG) scans are presented in **Figure 4-5** for bituminous marls OS-2, OS-3 and OS-4 with increasing total organic carbon (TOC) content and an organic-rich phosphorite (HOP-5) with the lowest TOC.

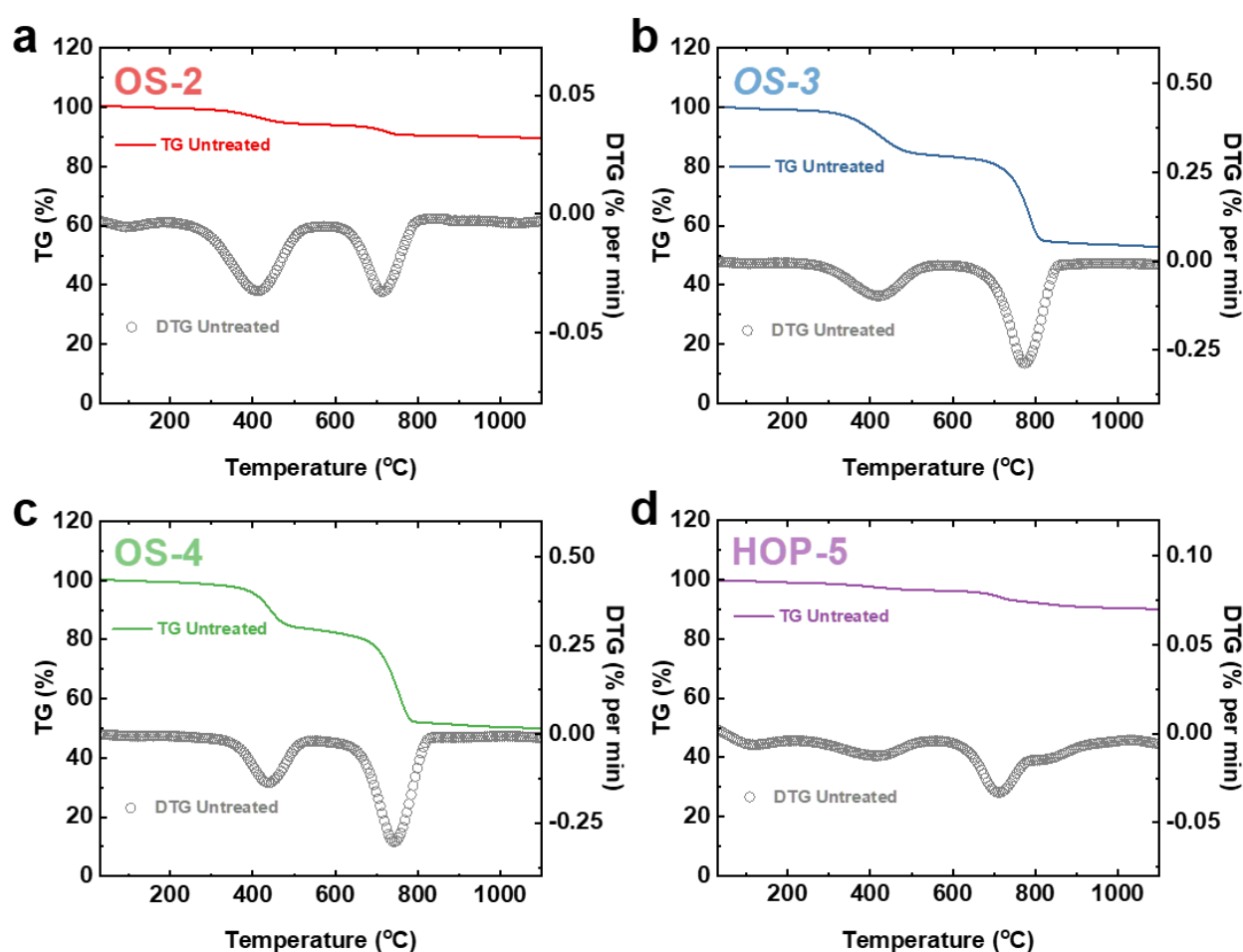


Figure 4-5. Thermogravimetry and derivative thermogravimetry (TG-DTG) from 30°C to 1100°C at a scan rate of 10°C/min in argon, (a) OS-2, (b) OS-3, and (c) OS-4, and (d) HOP-5.

The DSC calorimetry scans and MS spectroscopic data are presented in **Figures 4-6** and **4-7** respectively. The mass spectrometry peaks in **Figure 4-7** for atomic masses $m/z = 18$ and $m/z = 44$ indicate the presence in the samples of H_2O and CO_2 respectively. The interpretation of these techniques is well suited to parallel analysis and will be discussed together.

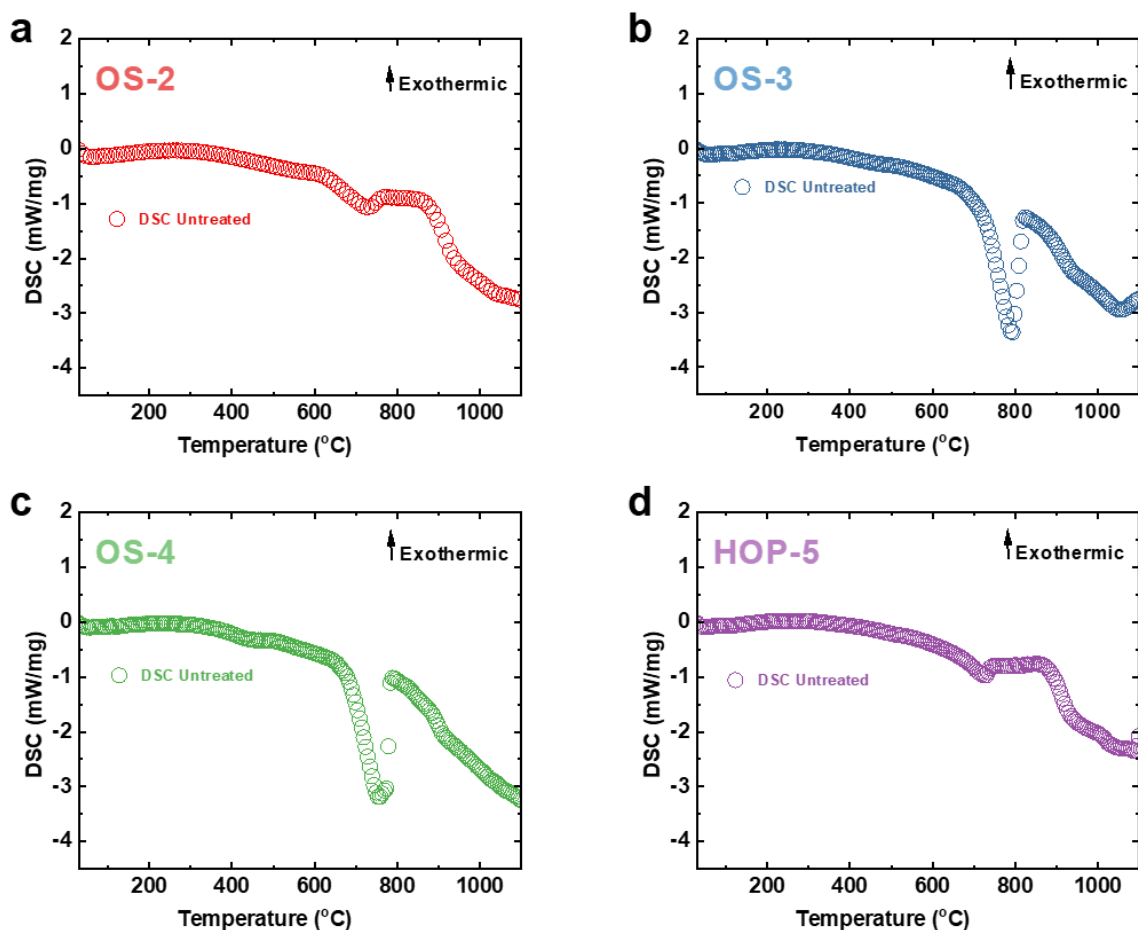


Figure 4-6. Differential scanning calorimetry (DSC) from 30°C to 1100°C at a scan rate of 10°C/min in argon; (a) OS-2, (b) OS-3, and (c) OS-4, and (d) HOP-5.

The thermal decomposition data show that over the temperature range examined we can distinguish three independent decomposition stages:

- **The first stage**, which occurs between 25°C and 200°C is similar for samples OS-2, OS-3, and HOP-5, and represents a small weight loss (~2 wt.%) attributed to the loss of adsorbed water. Weakly adsorbed surface waters are removed at 100°C, evidenced by the mass spectrometry H₂O peaks of OS-2, OS-3, and HOP-5. Carbonate marl OS-4, the most organic carbon-rich sample, does not show a detectable amount of weakly adsorbed water loss in the MS data. During the first stage any available light organics such as methane gas in kerogen pores are removed. However, no light organics are evidenced in the MS data. They are expected to be very low and might have been lost during the disaggregation process and dry storage.
- **The second stage**, which occurs between 200°C to 550°C (**Figure 4-5**) is attributed to kerogen pyrolysis. During pyrolysis, the breakdown of the complex organics occurs,

leaving behind coked carbon. The observed weight loss during the pyrolysis stage is consistent with the corresponding total organic content (TOC) of the sample. Considerable weight loss (~13 wt.% for both) events occur for the higher organic carbon content (TOC) samples OS-3 and OS-4, whereas for lower TOC samples OS-2 and HOP-5, the weight losses are only 5 wt.% and 2 wt.% respectively. The DTG data allows a more straightforward visual interpretation of the rate of weight loss events as this method shows broad peaks indicating that the decomposition events associated with pyrolysis have kinetic or transport limitations. The pyrolysis event is only weakly endothermic, as seen on the DSC data (**Figure 4-6**). During this stage, tightly confined water in pore networks, including amorphous organic carbon phase pores, are removed between 250°C to 500°C, as evidenced by the MS data (**Figure 4-7**). This is a function of the confinement effect of small pores trapping water as well as possible kerogen or bitumen decomposition, allowing previously inaccessible pores to release water.

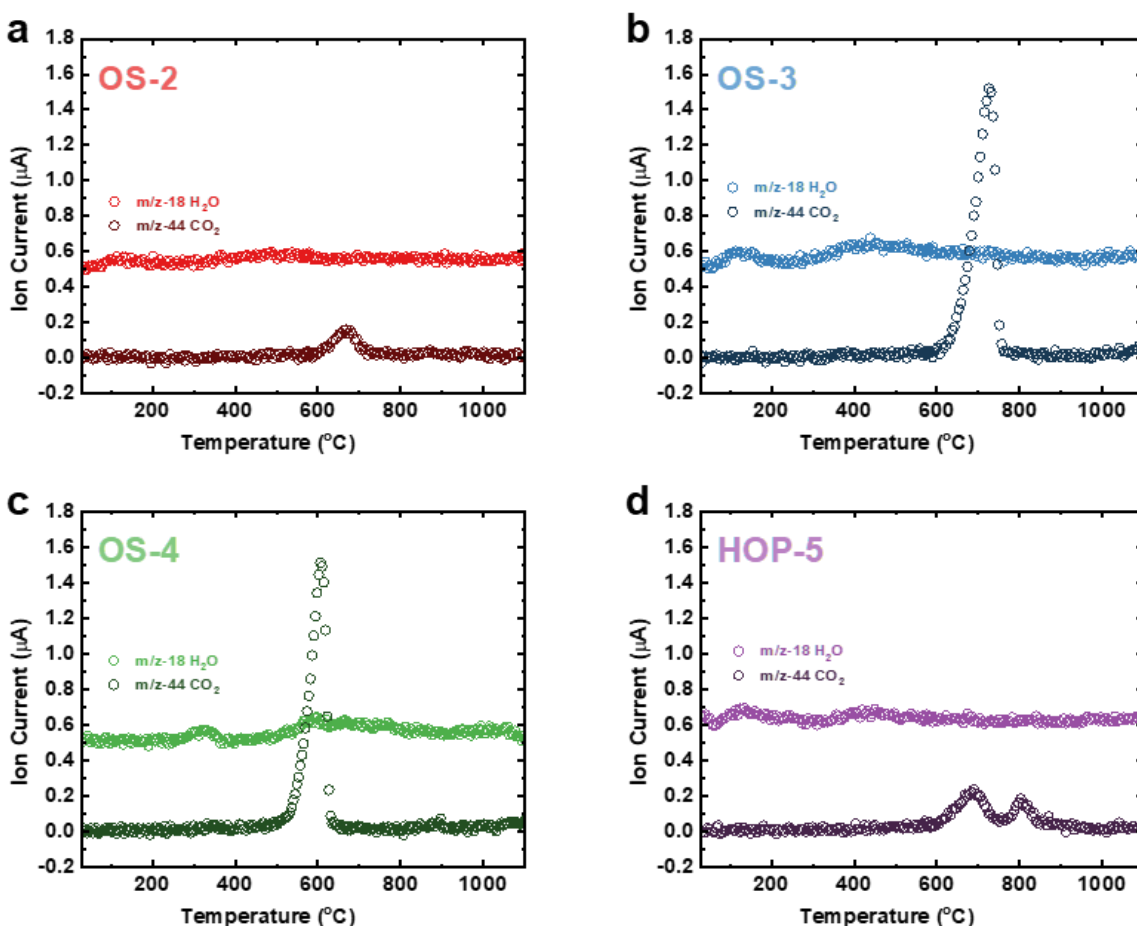


Figure 4-7. Mass spectrometry from 30°C to 1100°C at a scan rate of 10°C/min in argon, (a) OS-2, (b) OS-3, and (c) OS-4, and (d) HOP-5.

- **The third stage**, which occurs between 500°C to 1100°C is attributed to the decomposition of carbonate minerals calcite and/or dolomite. The events for OS-2, OS-3, and OS-4 are similar. Weight loss occurs above 550 °C, accelerating rapidly above 750°C as evidenced by the DTG (**Figure 4-5**) and a narrow endothermic DSC peak (**Figure 4-6**). These events are mirrored by MS detection (**Figure 4-7**) of inorganic CO₂ peaks. Decarbonization of calcite is complete around 800°C and involves the breakdown reaction for calcite:



The mass loss of CO₂ gas in this step (OS-2 = 4 wt.%, OS-3 = 30 wt.%, and OS-4 = 32 wt. %), is directly proportional to the modal abundance of calcite in these samples as determined by qXRD analysis.

Interestingly, the organic-rich phosphorite sample HOP-5 displays DTG, DSC, and MS CO₂ peaks centered at 750°C and a second MS-CO₂ peak above 800°C (**Figure 4-7**). The lower temperature, endothermic MS-CO₂ peak is associated with the decomposition of calcite. However, a higher temperature DTG inflection with a broad right shoulder DSC endothermic peak is associated with a second MS CO₂ peak above 800°C. This indicates the presence of another carbonate phase. XRD data suggests that this is related to the decomposition of carbonated calcium phosphate apatite (Ca₁₀(PO₄)₆(CO₃)_x(OH)_{2-2x}, with 0 ≤ x ≤ 1), known to occur in two steps in the temperature range 650 °C to 950 °C and associated with a mass loss of between 4 and 8% (Lafon *et al.*, 2003). The weight loss from all carbonate species in HOP-5 is 6 wt.%.

Though more work is required, we propose that the combined use of crystallographic and spectroscopic analyses with a thermal analysis provides important insights into the thermal stability and decomposition of the bituminous marl and organic-rich phosphorite samples.

4.2.5 Phase Stability and Thermally-induced Microstructural and Mineralogical Phase Changes

Microstructural characterization, temperature-dependent phase stability, and mineral phase changes involved the use of (i) in-situ XRD, (ii) in-situ DRIFTS as a function of temperature. The thermal behavior of inorganic crystalline phases contained in samples OS-2, OS-3, OS-4, and HOP-5 was tracked by in-situ during thermal ramping by tracking the in-situ XRD pattern of the material as a function of temperature from ambient temperature to 1000°C.

These 2D XRD pattern results are presented in **Figure 4-8**, **Figure 4-9**, **Figure 4-10**, and **Figure 4-11**. We also used 2D and 3D surface plots to better visualize temperature-dependent trends (**Figure 4-12**).

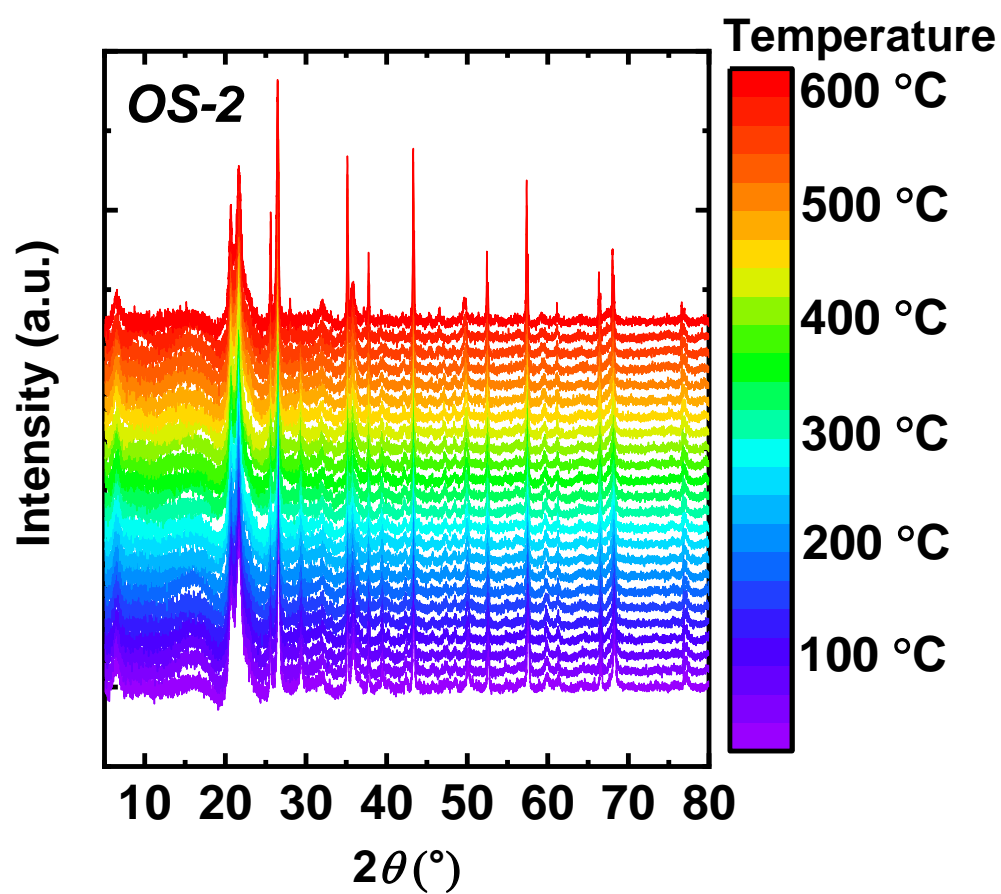


Figure 4-8. In-situ X-ray diffraction (in situ XRD) pattern of OS-2, range of 2θ of 5-80°, from 35°C to 600°C in argon.

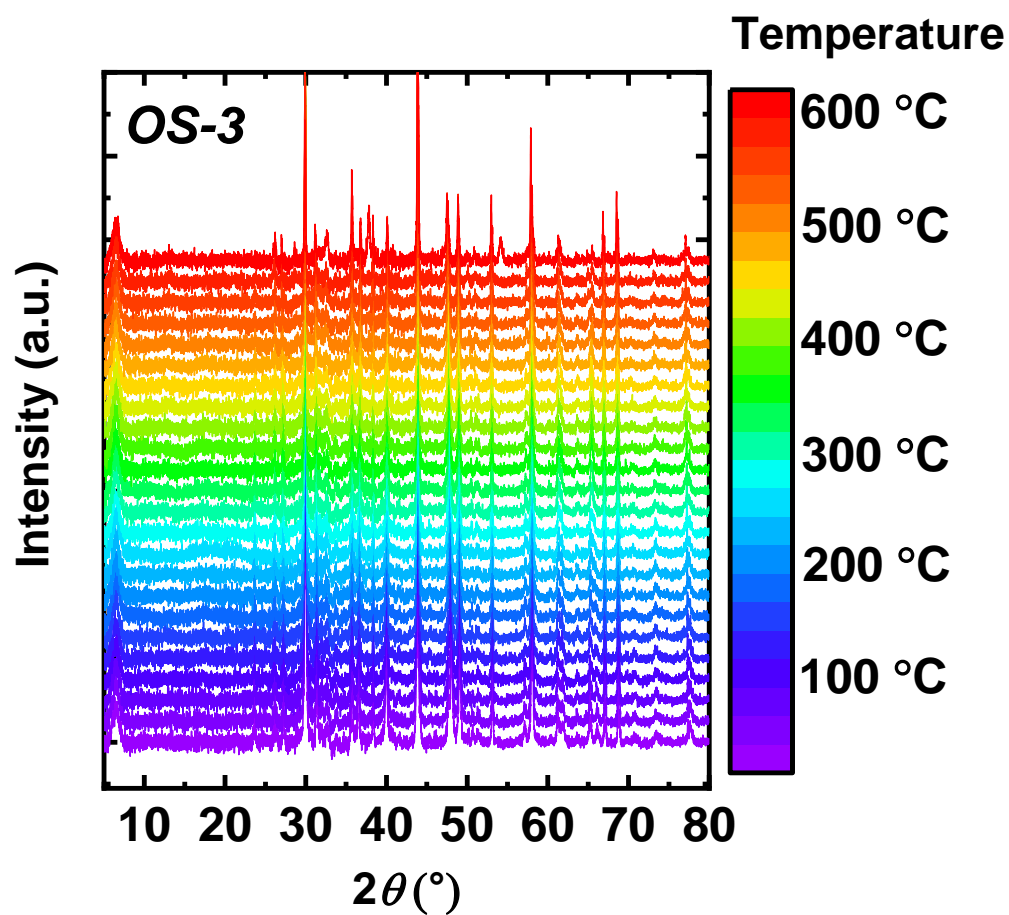


Figure 4-9. *In-situ* X-ray diffraction (in situ XRD) pattern of OS-3, range of 2θ of 5-80°, from 35°C to 600°C in argon.

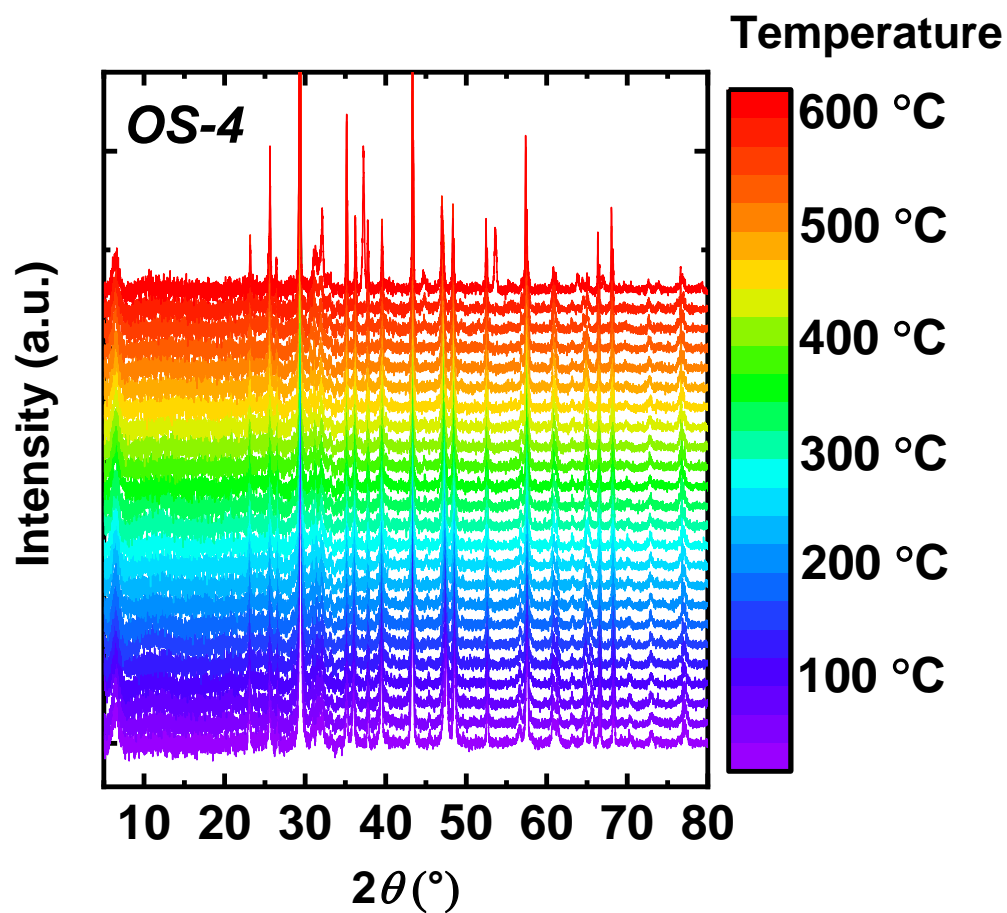


Figure 4-10. *In-situ* X-ray diffraction (in situ XRD) pattern of OS-4, range of 2θ of 5-80°, from 35°C to 600°C in argon.

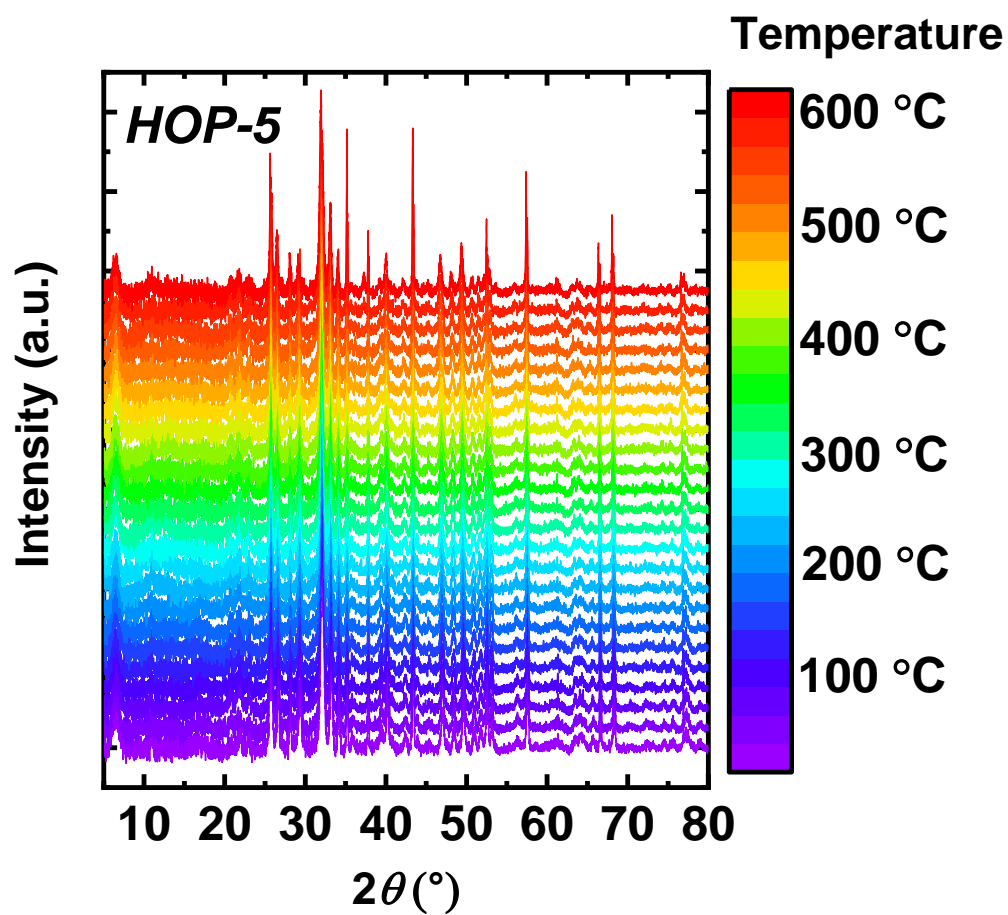


Figure 4-11. In-situ X-ray diffraction (in situ XRD) pattern of HOP-5, range of 2θ of 5-80°, from 35°C to 600°C in argon.

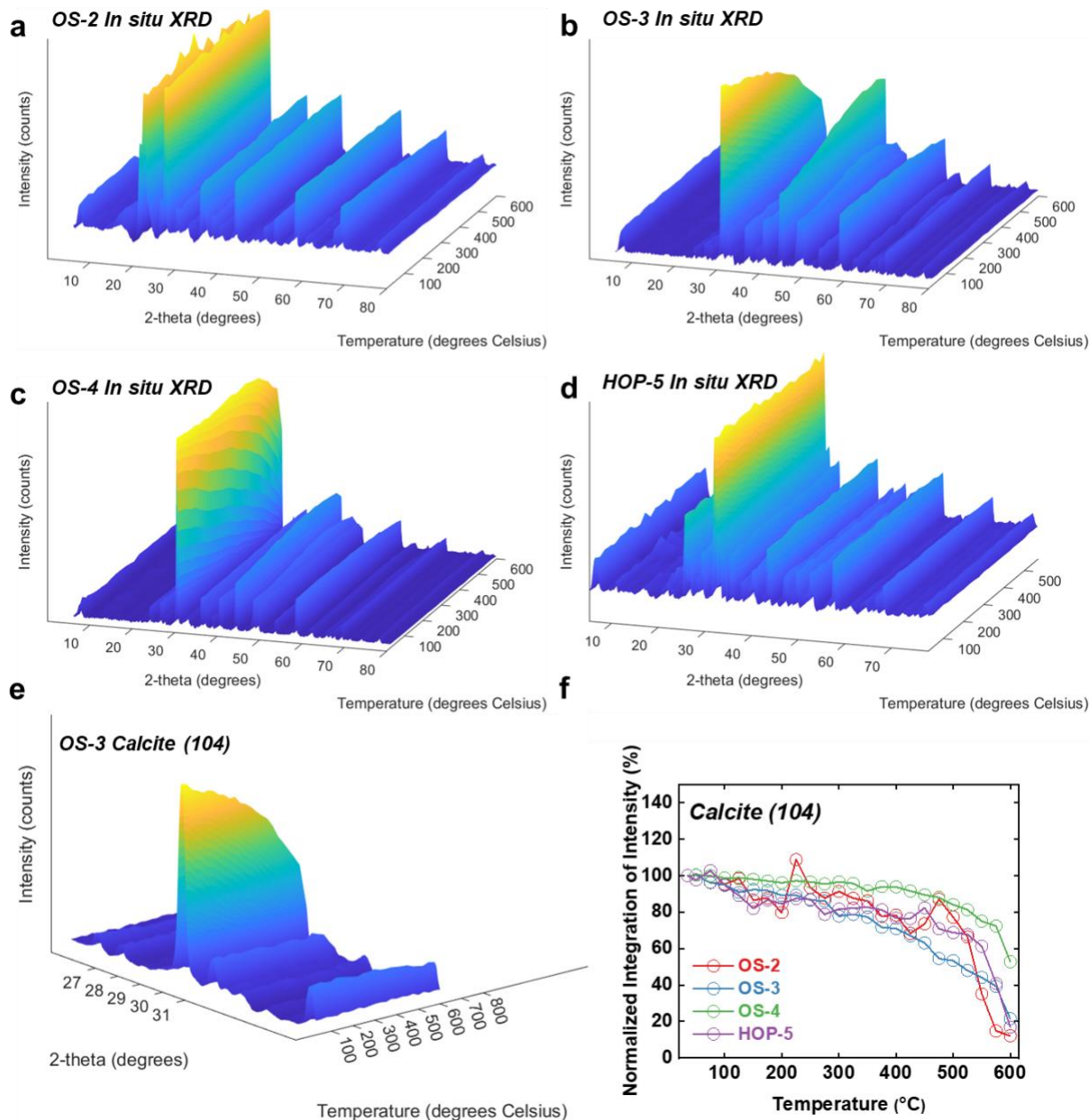


Figure 4-12. 3D plots of in-situ X-ray diffraction (in-situ XRD) patterns, 2θ of 5–80°, from 35°C to 600°C in argon: Samples OS-2 (a), OS-3 (b), OS-4 (c), and HOP-5 (d); (e) 3D plot of 2θ of 26°–35° showing the OS-3 (104) peak for calcite ($\text{CaCO}_3 = 54 \text{ wt.}\%$); (f) Normalized integration of intensity (NII) from all the samples (104) peak for calcite.

From these results we see that quartz undergoes a high temperature phase transition from α -quartz ($P3_221$) to *cristobalite* (β -quartz) ($P6_422$) at $\sim 573^\circ\text{C}$. The phases of carbonated calcium fluorapatite (HOP-5) and cristobalite (OS-2), do not experience significant changes below 600°C . Calcite is expected to breakdown in the temperature range measured by the *in-situ* XRD method, however carbonated fluoroapatite decomposes at higher temperatures based on composition

(Lafon *et al.*, 2003). All samples contain at least some calcite, CaCO_3 = 4 wt% (HOP-5), 9 wt.% (OS-2), 54 wt.% (OS-3), 53 wt.% (OS-4). Though calcite typically decomposes at temperatures above 600 °C with accelerated breakdown at higher temperatures up to 750°C, our experience from a previous study investigating calcite decomposition of a kerogen-rich Marcellus shale, indicates that calcite decomposition is detectable by *in-situ* XRD at temperatures as low as 560°C. This is due to the kinetics of calcite decomposition. In this study, we track calcite's decomposition by using the representative peak (*104*) located at $2\theta = 29^\circ$.

In **Figure 4-12(e)**, we show the 3D surface plot (*104*) peak for calcite in sample OS-3 to help visualize the intensity change, related to weight percentage, as a function of temperature.

To better understand the decomposition of calcite, we integrated the intensity of the (*104*) peak at each temperature, then normalized the integration of intensity (NIoI) as a percentage of the first integration from the initial scan at near-room temperature (35°C). The NIoI is correlated with the total amount of the phase present, shown as a function of temperature in **Figure 4-12(f)**. The NIoI for all samples displays a similar trend: (1) stable NIoI up to 400°C, (2) slight decrease of NIoI from 400°C to 500°C, and (3) rapid decrease in NIoI above 500°C. OS-2, OS-3, and HOP-5 show significant NIoI decrease (>50 %) up to 600°C. The decomposition of calcite occurs at lower temperatures than expected from the literature. We attribute this to two things; first, the long heating times occurred during the sequential scanning at every 25°C, and second, we cannot rule out leaks in the *in-situ* heating stage. Therefore, an oxidizing environment may contribute to lowering the decomposition temperature. We verified the decomposition of calcite using evidence from the formation of CaO at 600°C and the appearance of representative peaks (*111*), (*200*), and (*220*) at $2\theta = 33^\circ$, 38° , and 54° , respectively. The formation of CaO is only evidenced in OS-3 and OS-4 at 600°C, presumably due to a larger initial calcite content. When cooled to room temperature and in the presence of water, CaO will spontaneously hydrate to $\text{Ca}(\text{OH})_2$. Our *in-situ* XRD phase analysis will be explored further in FY22-23 as integrated with other techniques discussed, it lays the foundation for better understanding the phase stability and thermally-induced microstructural and mineralogical phase transformations in Negev bituminous carbonate lithologies.

4.2.6 Chemical Reaction By-products of Bituminous Negev Carbonates During Progressive Heating

It is of vital importance to understand the effect of IBD thermal loading and radiation on the potential generation and mobilization of fluids (liquid and gas phases) in the subsurface. In addition to new chemical and microstructural transformations, gas formation could lead to fracture formation and the modification of fluid pathways away from the disposal site. Experimental lab projects are being planned for FY22-23 that aim to address this issue and link it to potential natural barrier damage processes. In preparation for this work, we are investigating the use of *in-situ* DRIFTS from 35°C to 600°C to further track the formation of chemical by-products from the

thermal decomposition of Negev samples. **Figure 4-13** represents DRIFTS data for OS-2, OS-3, OS-4, and HOP-5.

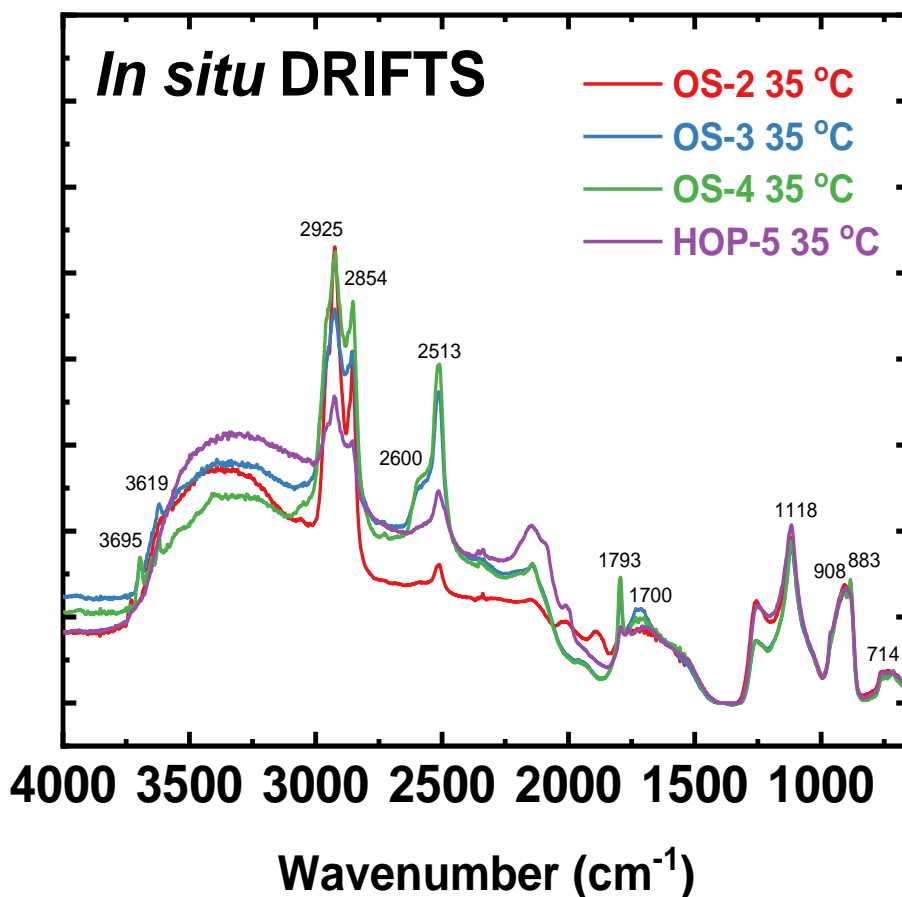


Figure 4-13. In-situ diffuse reflectance infrared Fourier transform spectroscopy (in-situ DRIFTS) spectra from 35°C to 600°C in helium for Negev bituminous carbonate samples OS-2 (a), OS-3 (b), OS-4 (c) and HOP-5 (d).

The DRIFTS spectra in **Figure 4-13** look identical for samples OS-3 and OS-4, and OS-2 in the spectrum range between 2700 cm^{-1} and 3000 cm^{-1} , and show a pair of strong absorption bands at 2925 cm^{-1} and 2854 cm^{-1} that are attributed to C-H stretching from organic matter. The intensity of the absorption bands is consistent with the sample's high total organic carbon content that varied from 9 wt% (OS-2) to 12 wt.% (OS-3) and 15 wt.% (OS-4). The intensity of these absorption bands is significantly reduced in HOP-5, which has a lower organic content ($\text{TOC} \leq 2 \text{ wt.}\%$).

At higher wave number there is also a broad shoulder between 3100 cm^{-1} and 3700 cm^{-1} present in all samples that is attributed to adsorbed water and stretching of hydroxyl groups associated with inorganic minerals such as clays and organic matter.

There are distinct sharp peaks at 3695 cm^{-1} , 3619 cm^{-1} associated with samples OS-3 and OS-4 that are not observed in OS-2 and HOP-5. These sharp peaks are attributed to the presence of clay minerals including Kaolinite, Montmorillonite, and Bentonite. A careful examination of the peak at 908 cm^{-1} indicates a distinct shoulder at 883 cm^{-1} that is present in OS-3 and OS-4 and absent in samples OS-2 and HOP-5 that is also a diagnostic peak for clay minerals. At lower wave number samples OS-3 and OS-4 have a very intense absorption band at 2513 cm^{-1} accompanied by a shoulder at 2600 cm^{-1} .

There is also a pair of absorption bands observed at 1793 cm^{-1} and 1700 cm^{-1} . These absorption features are characteristic of carbonate species, calcite, dolomite, and possibly carbonated fluoroapatite (Lafon *et al.*, 2003) and are also present in samples OS-2 and HOP-5 though less significantly. Sample OS-2 has the least amount of calcite or dolomite among the samples analyzed. The presence of the shoulder at 2600 cm^{-1} suggests that calcite predominates in these samples, which is supported by the XRD analyses. This absorption feature appears at slightly higher wave numbers in dolomite at 2600 cm^{-1} . However, the absorption peak at 883 cm^{-1} is shifted to higher wave numbers indicating the presence of some dolomite, mostly in the samples OS-3 and OS-4. This absorption band is present at 714 cm^{-1} for calcite.

The evolution of the drift spectra with temperature (**Figure 4-14**) for all samples indicate that there is a complete loss of water from the samples below 200°C . We also see significant transformation of the clay in samples OS-3 and OS-4 below 400°C , presumably due to the presence of montmorillonite, a hydrated sodium calcium aluminum magnesium silicate hydroxide $(\text{Na}, \text{Ca})_{0.33}(\text{Al Mg})_2(\text{Si}_4\text{O}_{10})(\text{OH})_2 \cdot n\text{H}_2\text{O}$, which has a modifiable structure that consists of free water molecules.

There is a continuous drop in the intensity of the absorption bands attributed to organic matter up to 600°C . Changes in the absorption bands attributed to calcite/dolomite are minor in the temperature range examined.

We are currently processing the data by integrating the area and intensity of different peaks to allow a more accurate analysis of the changes over the temperature range examined, however this technique appears promising in tracking the temperature-dependent changes in inorganic, organic and aqueous phases.

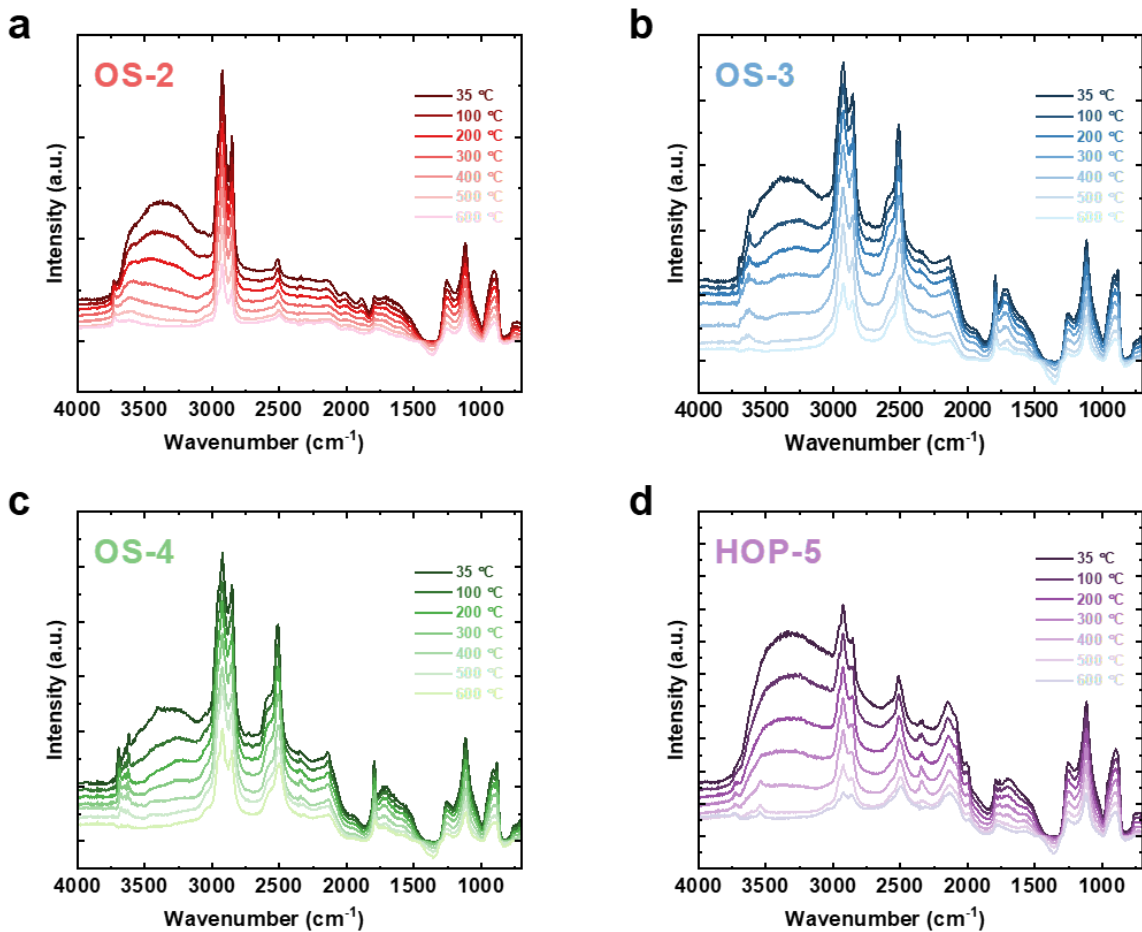


Figure 4-14. *In-situ* DRIFTS spectra from 35°C to 600°C in helium for Negev bituminous carbonate samples OS-2 (a), OS-3 (b), OS-4 (c) and HOP-5 (d).

5 Summary and Conclusions

Over a four-year period, we have accomplished building the first 3D NE Negev vadose zone flow and transport model including thermal forcing to represent heat generating nuclear waste. This involved six principal tasks:

- Characterizing the YP site subsurface to a depth of 500 meters,
- Completing investigative laboratory studies of uranium adsorption on key Negev shallow marine lithofacies assemblages (LFAs),
- Developing equilibrium and surface complexation uranium sorption models based on experimental results,
- Building a 3-D computational mesh of the Yamin Plain vadose zone,
- Completing multiple, flow and transport simulations to assess the potential effect of “wetter” future climate scenarios on ground saturation around an IBD disposal site and potential migration of subsurface contamination, and
- Adding a realistic thermal load to the intermediate depth borehole

All of these tasks have been successfully completed and the hydrologic and geochemical models have been calibrated, verified and validated with the caveat that the simulation results remain preliminary and can be greatly improved as more data becomes available.

The following initial conclusions are:

- The Late Cretaceous shallow marine rocks of the Mt. Scopus Group exhibit very high uranium sorption capacities, specifically the phosphorites and bituminous marls of the Mishash Fm. This potential “natural barrier” is the key to the containment of nuclear waste migration from an IBD waste disposal system.
- The buffering capacity of the shallow marine rocks is strong due to the presence of carbonate phases calcite (CaCO_3) +/- dolomite ($\text{MgCO}_3 \cdot \text{CaCO}_3$) in bituminous limestone marls, and carbonated fluoroapatites ($\text{Ca}_{10}(\text{PO}_4)_6(\text{CO}_3)_x(\text{OH})_{2-2x}$, with $0 \leq x \leq 1$) in fossiliferous phosphorites. This implies that when acidic contaminant waste fluids breach the waste packages the *in-situ* pH and alkalinity of the groundwater system will likely remain the same (alkaline) and prevent the aqueous uranium speciation from changing, so that the U-sorption capacity would remain high.
- The empirical single-site, non-electrostatic surface complexation model that was derived from the laboratory measurements was sufficient to replicate the sorption/desorption behavior of all four shallow marine rock types studied. It is therefore a promising predictive tool if used in conjunction with better site data.

- The shallow marine fossiliferous phosphorite assemblages have the highest U-sorption capacity ($K_d = 422 \pm 77$ L/kg) of any other rock type, associated with the presence of abundant fluoroapatite. The organic limestone marls ($K_d = 74.3 \pm 10.9$ L/kg) also have a potentially high U-sorption capacity associated with the presence of montmorillonitic clays, but its hydrophobicity and low permeability do not favor this rock as an effective porous media for mitigating contaminant flow. Conversely, the Hazeva Gr. sandstone is porous and has the highest permeability ($k = 200$ mD) and saturated conductivity values ($K_{SAT} = 2.3 \times 10^{-4}$ cm/s) of all rock samples measured, so that even though its laboratory-measured U-sorption capacity is relatively low compared to other samples, similar sandstones in the shallow marine sequence could potentially behave as a very effective barriers to U-contaminant migration.
- Site-scale simulations updated in FY21, designed to assess the potential impact of future climate change scenarios on IBD disposal indicate that:
 - For extreme 210 mm/y infiltration conditions, the nuclear inventory is swept out of the IBD near field domain (80 m x 100 m x 100 m) in just over 200 years.
 - For 30 mm/y infiltration conditions, the contaminant plume remains in the IBD domain even after 1000 years.
 - For ponding events and in the case of waste canister degradation, the initial uranium contaminant concentration that exists over the entire IBD domain, is entrained by the steady 0.1 mm/y current background flow field and escapes the nearfield domain after 700 years but at concentrations values that would likely be undetectable.
- Due to the preponderance of organic-rich rocks in the shallow marine Mishash Fm. we have initiated and completed recent exploratory tests in FY21, on the stability of organic carbon-rich lithologies such as the bituminous marls and organic phosphorites. Continued work will allow us to determine the critical breakdown temperature at which flammable fluids (liquid + gas) are generated and the effects of thermal IBD loading on physical and chemical properties of the natural barrier. The results are promising and extension of this study to radiation effects is planned for FY22-23.

Though subject to further change, drilling has been rescheduled to the spring of 2022 in an area located approximately one mile of borehole Y-9 used in this study. Based on data needs identified from our studies, we recommend that the drilling activities involve: (i) continuous core sample recovery from the top down to the base of the entire shallow marine sedimentary sequence, (ii) down hole logging, and (iii) hydrologic pump tests in key porous formations. Because of the paucity of data on ground water distribution, saturation and mineral and lithofacies distributions at depth this is crucial improving our models and simulation predictions.

In light of our findings, future work planned for FY22-23 will focus on (i) incorporating new experimentally-derived data parameters and equations on the thermal loading and radiation effects of nuclear waste IBD disposal, (ii) improving our Negev subsurface model predictions, and (iii) using data from a new exploratory borehole to update the model, if available. Regardless of the drilling schedule however, the LANL PFLOTRAN *Subsurface Northeastern Negev 3D Process Model* will continue to be improved and updated so as to serve as the scientific basis for and support the Sandia PFLOTRAN *Performance Assessment* model to be used in the IBD nuclear waste disposal site *Safety Case*.

6 References

- Bauer, S., C. Choens, W. Kibikas, E. Shalev, and V. Lyakhovsky, 2021. Characterization and borehole analysis of the Ghareb Formation for nuclear waste disposal, 55th US Rock Mechanics/Geomechanics Symposium, ARMA 21-1662, Houston TX, June 20-23, 2021, 9 p.
- Birdsell, K.H., B.D. Newman, B.A. Robinson, and D.E. Broxton, 2005. Conceptual models of vadose-zone flow and transport beneath the Pajarito Plateau, Los Alamos, New Mexico. *Vadose Zone Journal*, 4, 620–636.
- Bussod, G.Y., P.H. Stauffer, H. Boukhalfa, M. Dangelmayr, S. Kuluris, N. Hayes-Rich, T.A. Miller, G. Woldegabriel, R. Rosenzweig, R. Calvo, N. Balaban, O. Klein-Ben David, A. Dody, 2020. 2017-2020 FINAL REPORT NNSA-IAEC SCIENCE AREA 5 ENVIRONMENTAL ISR, Los Alamos National Laboratory Report LAUR-20-28271, 115 p., October 15, 2020.
- Carter, J., Luptak, A., Gastelum, J., Stockman, C., Miller, A., 2013. Fuel Cycle Potential Waste Inventory for Disposition, FCR&D-USED-2010-000031 Rev. 6, U.S. Department of Energy, Used Fuel Disposition R&D Campaign.
- Kwicklis, E.M., A.V. Wolfsberg, P.H. Stauffer, M.A. Walvroord, and M.J. Sully, 2006. Multiphase Multicomponent Parameter Estimation for Liquid and Vapor Fluxes in Deep Arid Systems Using Hydrologic Data and Natural Environmental Traces, *Vadose Zone Journal*, 5, 934-950.
- Lafon, J-P, E. Champion, D. Bernache-Assollant, R. Gilbert, A-M. Danna, 2003. Thermal decomposition of carbonated calcium phosphate apatites, *Journ. Thermal Analysis & Calorimetry*, 72(3), 1127-34. doi:10.1023/A:1025036214044
- van Genuchten, M.T., F.J. Leij, and S.R. Yates, 1991. The RETC Code for Quantifying the Hydraulic Functions of Unsaturated Soils, Version 1.0. EPA Report 600/2-91/065, U.S. Salinity Laboratory USDA-ARS, Riverside, CA.

7 FY21 Meetings and Publications

7.1 Meetings and Publications

7.1.1 Annual Workshops

- Several meetings and teleconference calls have been held with Israeli organizers Gabi Bar-Nes (NRCN) and Ofra Klein-BenDavid (NRCN) to plan presentations for the upcoming **6th Annual 2021 IAEC-NNSA Virtual Workshop**.
- WM3 and WM7 Team members participated in, and gave presentations at the **5th Annual NNSA-IAEC Topic Area V Workshop** (Virtual) on November 10-11, 2020.
- LANL WM-3 and WM-7 Teams participated in the monthly to bi-monthly **NRCN Workshop on Negev Bituminous Lithologies Program** run by Ofra Klein-BenDavid and Noa Balaban (NRCN) to discuss new FY22 workscope aimed at understanding the thermal and radiation effects on bituminous marls and phosphates (kerogen breakdown) in the vicinity of a deep borehole waste package. Note that Meetings that were initiated in January 2021 have been suspended by organizers since July 2021 due to current events and related scheduling difficulties in Israel.
 - Based on the Workshop discussions, Negev bituminous rock samples were shipped to LANL in June 2021 by GSI, Jerusalem, Israel and are currently being experimented on by the geochemistry team.

7.1.2 Weekly and bi-Monthly Meetings

- Throughout the year weekly WEBEX meetings have been ongoing between LANL and GSI scientists to facilitate model and laboratory tests and field drilling updates, and assure the integration of collaborative efforts.
- Since June 2021 Gilles Bussod has been corresponding by phone and email with organic geochemists from GeoMark, Inc. (US) and Dr. Itay Reznik on the subject of potential experimental work at pressure and temperature that could improve our understanding of the effect of temperature on the decomposition and mobility of hydrocarbon phases in organic-rich Negev carbonates.
- This past summer Hakim Boukhalfa has engaged researchers from Washington State University and explored options for irradiating the organic-rich Negev samples to examine effects of radiation and thermal loading on their microscopic and macroscopic structures. There is an option to irradiate samples at WSU in collaboration with Dr. Di Wu, which gives us access to the WSU experimental reactor to start experiments soon.

7.1.3 Publications

Geochemistry Manuscript:

- Dangelmayr, M.A., Bussod, G.Y., Reimus, P.W., Boukhalfa, H., Woldegabriel, G., Xu, H., Harris, R., Stauffer, P., Klein-BenDavid, O., Balaban, N., Calvo, R., and Rosenzweig, R. (2022). Uranium Sorption Capacity of Upper Cretaceous Shallow Marine Lithologies, Negev desert, Israel, Science of the Total Environment, Los Alamos National Laboratory Report [LA-UR-21-26182] (To be submitted after revision, November 2021)

Negev Hydrogeochemical Modeling Manuscript:

- Stauffer *et al.* (2022). Assessment of Contaminant Migration for Intermediate Borehole Disposal Site, Northeastern Negev desert, Israel - *Vadose Zone Journal* (To be submitted, January, 2022).

Annual Reports:

- Bussod, G.Y., P.H. Stauffer, H. Boukhalfa, M. Dangelmayr, S. Kuluris, N. Hayes-Rich, T.A. Miller, G. Woldegabriel, R. Rosenzweig, R. Calvo, N. Balaban, O. Klein-Ben David, A. Dody, 2020. 2017-2020 FINAL REPORT NNSA-IAEC SCIENCE AREA V ENVIRONMENTAL ISR, Los Alamos National Laboratory Report [LAUR-20-28271], 115 p., October 15, 2020.